UNIVERSIDAD DE CHILE
FACULTAD DE CIENCIAS FÍSICAS Y MATEMÁTICAS
DEPARTAMENTO DE ASTRONOMIA

MAJOR MERGERS AT $z \simeq 4.8$

TESIS PARA OPTAR AL GRADO DE MAGISTER EN CIENCIAS MENCION EN ASTRONOMIA

NATHEN HUY NGUYEN

PROFESOR GUÍA:
PAULINA LIRA TEILLERY

MIEMBROS DE LA COMISIÓN:
ROBERTO J. ASSEF TREBILCOCK
EDUARDO HARDY RASKOVAN
RENÉ A. MÉNDEZ BUSSARD

SANTIAGO DE CHILE
2020

SUMMARY OF THESIS FOR THE DEGREE OF MASTER OF SCIENCE IN ASTRONOMY

MAJOR MERGERS AT Z $\simeq$ 4.8

In this thesis I will present an expanded study of quasars at high-redshift, which have been observed with the Atacama Large Millimeter Array (ALMA). We search for nearby companions to our quasars in [C II] $\lambda 157.74\,\mu$m and the nearby underlying continuum for companion galaxies. which we believe will act as a common reservoir of gas to fuel both Star Formation (SF) and Super Massive Black Hole (SMBH) growth. In the first chapter I briefly introduce the basic concepts and motivations of this thesis.

In the second chapter I expand on the sample selection and the previous observations carried out on the quasars presented in this thesis. ALMA observations have been carried out using the [C II] $\lambda 157.74\,\mu$m line and nearby underlying continuum. This allows the detection of accompanying Sub-Millimeter Galaxies (SMGs), which are confirmed by matching redshifts to that of the quasar. I find that five of the eighteen Active Galactic Nuclei (AGN) have nearby companions which is $\sim 28\%$ of the sample. No AGN has more than one companion.

Then, in the third chapter, I begin analysis of the [C II] line and continuum. Because ALMA provides us spectral data cubes, it is possible to use Line of Sight Velocity Distribution (LOSVD) to construct velocity maps of the host galaxies and SMGs. With these velocity maps I describe the morphologies and kinematics of the host galaxies. By using the underlying continuum I construct a possible Spectral Energy Distribution (SED) of the host galaxies, from which is it possible to calculate Star Formation Rates (SFRs). The quasar hosts have a SFR rate of $\sim 90 - 3200\,M_{\odot}\,\mathrm{yr}^{-1}$, while the companions are forming $69 - 542\,M_{\odot}\,\mathrm{yr}^{-1}$. Once the luminosity of the SF is calculated, it is possible to compare it to the bolometric luminosities of our quasars, comparing the growth of the AGN and host galaxies to the robust L_{AGN} vs. L_{SF} relation found in the literature.

In the fourth chapter it is possible to use the previously mentioned measurements and host galaxy properties to calculate the dynamical, dust, and gas masses of the AGN host galaxies and companion SMGs. Assuming $f_{gas} = M_{gas}/M_{\mathrm{dyn}} = 0.6$ we are able to derive an estimate of the stellar mass $M_{\star} = 0.4\ M_{\mathrm{dyn}}$, thus I am able to compare the observed objects to the Main Sequence (MS) of high-redshift galaxies. In this chapter I explain that the detected objects sit above the expected MS positions.

Finally in the fifth chapter, I detail how it is possible to predict the possible growth of the AGN and host galaxies using derived stellar masses ($M_{\star}$) and SFRs, as well as black hole masses and accretion rates derived in Trakhtenbrot et al. (2011). The results indicate that while the SMBHs will grow to be greater than or equal to the mean mass of local SMBHs, the M_{BH}/M_{*} ratio will be lower than locally observed ratios. In the end of this chapter I attempt to explain in detail the possible merger driven scenario presented in the data.

RESUMEN DE TESIS PARA OPTAR AL GRADO DE MAGÍSTER EN CIENCIAS MENCIÓN ASTRONOMÍA

MAJOR MERGERS AT Z $\simeq$ 4.8

En esta tesis presentaré un estudio extendido de cuásares a alto redshift, que han sido observados con el Atacama Large Millimeter Array (ALMA). Buscamos compañeros cercanos a nuestros cuásares en [C II] $\lambda 157.74\,\mu$m y en el continuo para galaxias compa$\sim$neras, las cuáles creemos que funcionarán como una reserva común de gas para alimentar tanto formación estelar como crecimiento de agujeros negros supermasivos. En el primer capítulo introduciré brevemente los conceptos básicos y motivaciones tras esta tesis.

En el segundo capítulo, hablaré de la selección de muestras y observaciones previas de los cuásares presentados en esta tesis. Observaciones con ALMA se han realizado usando la línea de [C II] $\lambda 157.74\,\mu$m y el continuo cercano. Esto permite la detección de galaxias submilimétricas acompañantes, las que son confirmadas haciéndolas coincidir con el redshift del cuásar. Se observa que cinco de dieciocho Núcleos Activos de Galaxias (AGN) tienen compañeros cercanos, lo que corresponde a un $\sim$ 28% de la muestra. Para ningún AGN observamos más de un compañero.

En el tercer capítulo, comenzamos el análisis de la línea de [C II] y el continuo. Debido a que ALMA no entrega cubos de datos, es posible utilizar la distribución de velocidad en la línea de visión (LOSVD) para construir mapas de velocidad de las galaxias huésped y SMGs. Con estos mapas de velocidad describimos la morfología y cinemática de las galaxias huésped. Utilizando el continuo construimos una posible distribución espectral de energía (SED) para las galaxias huésped, a partir de la cual es posible calcular las tasas de formación estelar (SFRs). Los huéspedes del cuásar tienen un razon SFR de $\sim 90 - 3200\,M_\odot\,\mathrm{yr}^{-1}$, mientras que los compañeros forman $69 - 542\,M_\odot\,\mathrm{yr}^{-1}$. Una vez que la luminosidad de SF es calculada, es posible compararla con las luminosidades bolométricas de nuestros cuásares, comparando el crecimiento de las AGN y galaxias huésped con la relación L_{AGN} vs. L_{SF} que se encuentra en la literatura.

En el cuarto captítulo es posible utilizar las mediciones previamente mencionadas, junto con las propiedades de las galaxias huésped para calcular las masas dinḿicas de polvo y gas de las galaxias huésped de AGN y compañeras SMGs. Asumiendo $f_{gas} = M_{gas}/M_{\mathrm{dyn}} = 0.6$ derivamos un estimado para la masa estelar $M_\star = 0.4\ M_{\mathrm{dyn}}$, y de esta forma comparamos los objetos observados con la secuencia principal (MS) de galaxias a alto redshift. En este captítulo explico que los objetos detectados se ubican sobre la posición esperada en la MS.

Finalmente, en el quinto capítulo, detallo como es posible predecir el crecimiento de AGN y galaxias huésped utilizando masas estelares ($M_\star$) y SFRs derivadas, junto con las masas de agujeros negros y tasas de acreción derivados en Trakhtenbrot et al. (2011). Los resultados indican que si bien los SMBHs crecerán hasta tener masas mayores o igual que la masa media de SMBHs locales, la razón M_{BH}/M_* será menor a las razones observadas localmente. Al final de este capítulo intentamos explicar en detalle un escenario de *merger* presentado en los datos.

To my friends and family.

Contents

List of Tables

List of Figures

Chapter 1

Introduction

It is generally agreed upon that most galaxies host Super Massive Black Holes (SMBHs) of mass $10^6 - 10^9\ M_\odot$ at their center (Kormendy & Ho, 2013). When these SMBHs experience rapid growth due to inflow of gas and stars the accretion of said material will cause massive amounts of emission (Salpeter, 1964), we call this phase of luminous activity an Active Galactic Nuclei (AGN). AGNs can be relatively bright sources with luminosites as large as 10^{47} erg s^{-1} dominating over a wide spectral range from radio to the hard x-ray (Hopkins et al., 2007). Because of this, AGN serve as a fantastic means to study the high-redshift universe, with quasars being discovered up to $z = 7.54$ (Venemans et al., 2017; Banados et al., 2018).

Locally, galaxies exhibit tight correlations between their central SMBH mass ($M_{\rm BH}$) and the stellar velocity dispersion (σ_*) of the host bulge of the SMBH, referred to as the $M_{\rm BH} - \sigma_*$ relation (Ferrarese & Merritt 2000, see Figure 1.1). The $M_{\rm BH} - \sigma_*$ relation suggests that the AGN affects its local and host-galaxy environment, while the reverse might also be true, the local and host-galaxy environment influences the AGN. Energetic AGN activity can produce outflows such as winds (Silk & Rees, 1998; Nesvadba et al., 2008) or relativistic jets (Allen et al., 2006) which can suppress star forming activity and inflowing material. Therefore it is expected that AGN activity has a significant impact on the star formation processes as the host galaxy evolves. Numerical simulations show that the AGN energy input plays a primary role in regulating the growth and activity of the central SMBHs and their host galaxies (Di Matteo et al., 2005; Hopkins et al., 2006, 2008). This common evolution between the AGN and its host can be seen in Figure 1.1, where we see the peak of SF-history coincides with the peak of black hole accretion history at $z \sim 2$.

If we were to consider the relation of the luminosities associated with SF ($L_{\rm SF}$) with SMBH accretion ($L_{\rm AGN}$), there are two cases. The first is the "SF-dominated" scenario where $L_{\rm SF} > L_{\rm AGN}$ with the two properties being uncorrelated (Shao et al., 2010; Rosario et al., 2012). The second case is the "AGN-dominated" scenario where $L_{\rm AGN} > L_{\rm SF}$. In this case the sources appear to be correlated around a power-law line (as seen in Figure 1.3) which is given roughly by $L_{\rm SF} \simeq 10^{43}(L_{\rm AGN}/10^{43}\,{\rm erg\,s^{-1}})^{0.7}$ (Netzer, 2009; Lutz et al., 2010). The difference between these two cases is most likely due to sample bias and the difference in AGN duty cycles and that SF time-scales, which will be discussed in more detail in later Chapters. This relation

implies that the phase of intense SMBH growth occurs concurrently with intense SF activity, reaching star formation rates (SFRs) of $\sim 1000\ M_{\odot}\,\mathrm{yr}^{-1}$ for SMBHs with $\dot{M}_{\mathrm{BH}} \sim 15\ M_{\odot}\,\mathrm{yr}^{-1}$ (i.e., $L_{\mathrm{AGN}} \sim 10^{47}\,\mathrm{erg\,s}^{-1}$). It stands to reason that both processes are pulling from a shared reservoir of cold gas. These reservoirs of cold gas are commonly proposed to be fed by major mergers in the brightest AGN and more powerful starburst galaxies (Di Matteo et al., 2005; Hopkins et al., 2006; Somerville et al., 2008). It is the search for evidence of these major mergers which motivates this thesis work.

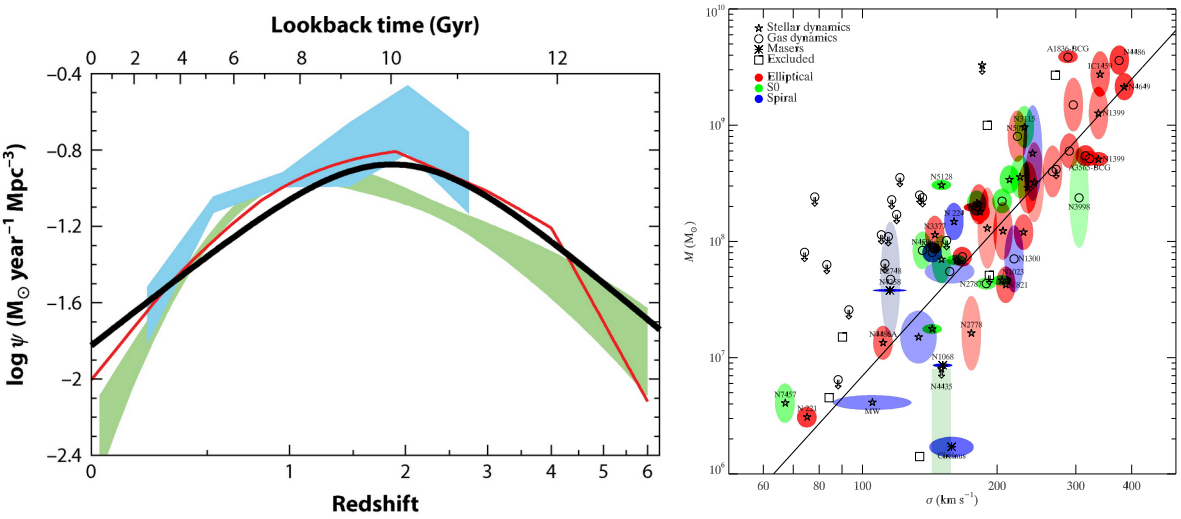

Figure 1.1: **LEFT:** Figure 15 of Madau & Dickinson (2014); This plot compares the best-fit star-formation history (black curve) and the accretion history of massive black holes derived from X-ray observations (red line from Shankar et al. (2009) and light green shading from Aird et al. (2010)) and infrared observations (light blue shading from Delvecchio et al. (2014)). The radiative efficienecy is set to $\varepsilon = 0.1$. The comoving rates of black hole accretion havae been scaled up by a factor of 3,300 for visual comparison to the star-formation history. **RIGHT:** The $M_{\mathrm{BH}} - \sigma_{*}$ relationship for galaxies with dynamical measurements from Gültekin et al. (2009). The symbol indicates the method of BH mass measurement: stellar dynamical (pentagrams), gas dynamical (circles), masers (asterisks). The color of the error ellipse indicates the Hubble type of the host galaxy: elliptical (red), S0 (green), and spiral (blue). The line is the best fit relation to the full sample.

Testing these scenarios observationally has proven to be extremely challenging since it requires characterizing accreting SMBHs and their hosts for well defined samples. In powerful quasars the AGN-related emission dominates over most of the optical-NIR spectral regime, significantly limiting the prospects of determining the host properties, while the high redshift severely limits which robust lines can be used to measure M_{BH}. This leads to the 'islands' of possible samples we see in Figure 1.2, with complete samples already studied at $z \sim 2.4$ and $z \sim 3.3$, and several different but less thorough studies at $z > 6$. Trakhtenbrot et al. (2011) used the observations of the Mg II λ2798 emission line and nearby 3000 Å continuum to construct a viable sample at $z \sim 4.8$. This redshift is an important cosmological epoch, situated near the end of the epoch of reionization at $6 < z < 10$ (Planck Collaboration et al., 2016), and when the most massive SMBHs are growing at the fastest rates to reach their final masses ($M_{\mathrm{BH}} > 10^{10} M_{\odot}$) before $z \sim 2$ (Trakhtenbrot et al., 2011; Trakhtenbrot & Netzer, 2012; De Rosa et al., 2014). In addition the [C II] line, which is a strong line that

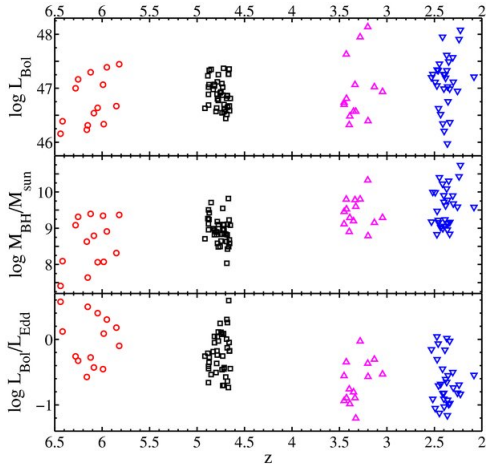

Figure 1.2: From Trakhtenbrot et al. (2011). $L_{\rm bol}$, $M_{\rm BH}$, and $L/L_{\rm Edd}$ vs. redshift, for samples of different redshifts: black squares for the $z \simeq 4.8$ sample originally presented in presented Trakhtenbrot et al. (2011), magenta triangles for the $z \sim 2.4$ sample of Shemmer et al. (2004), blue triangles for the $z \sim 3.3$ sample of Netzer et al. (2007), and red circles of the combined samples of Kurk et al. (2007) and Willott et al. (2010).

can be used to determine galaxy properties at high-redshift (Pentericci et al., 2016) and has a measured transition frequency of 1900.537 GHz, is reliably observable from the ground at $4.5 \simeq z \simeq 8.5$ using band six and seven of the Atacama Large Millimeter Array (ALMA), and lower redshift in bands. Therefore [C II] can also be observed for the sample of quasars constructed in Trakhtenbrot et al. (2011).

We probe the connection between SMBHs and their host galaxies using an optically selected, flux-limited sample of the most luminous quasars at $z \sim 4.8$. These fast-growing SMBHs should also be experiencing fast stellar growth, as seen in high-$L_{\rm AGN}$ systems studied at $z \sim 1-3$ (Netzer et al., 2007; Rosario et al., 2012; Lutz, 2014). The best approach is to observe these systems in the far-IR (FIR), where dust heated by starformation dominates the continuum emission and interstellar emission lines allow us to determine the host kinematics. As already discussed, this can be readily achieved through the ALMA sub-mm observations. Throughout this work we assume a cosmological model with $\Omega_\Lambda = 0.7$, $\Omega_{\rm M} = 0.3$, and $H_0 = 70\,{\rm km\,s^{-1}\,Mpc^{-1}}$, which provides an angular scale of about $6.47\,{\rm kpc}/''$ at $z = 4.8$, the typical redshift of our sources.

This thesis work is composed primarily of the work done in Nguyen et al. (2020), where the cycle-4 data has been reduced and analyzed. In this thesis we compile all the results of the cycle-4 and cycle-2 (Trakhtenbrot et al., 2017) data together in order to present a coherent sample.

In **Chapter 2** we describe our data sample and methods of data reduction and analysis. We examine in detail our detections and the significance of our possible companions. In Section **Chapter 3** we analyze the [C II] line and underlying continuum spectrum of our objects. We examine the direct results of analysing our spectrum, velocity maps and Spectral Energy Distributions (SEDs). In **Chapter 4** we determine the host properties; dynamical, dust, and gas masses, and compare them to the values found in the literature. In **Chapter 5**

we predict the possible SMBH vs. M_* growth, and theorize about the state of major mergers among our objects. Finally in **Chapter 6** we conclude our thesis, summarize the results and findings of our work, and list the important points to take away.

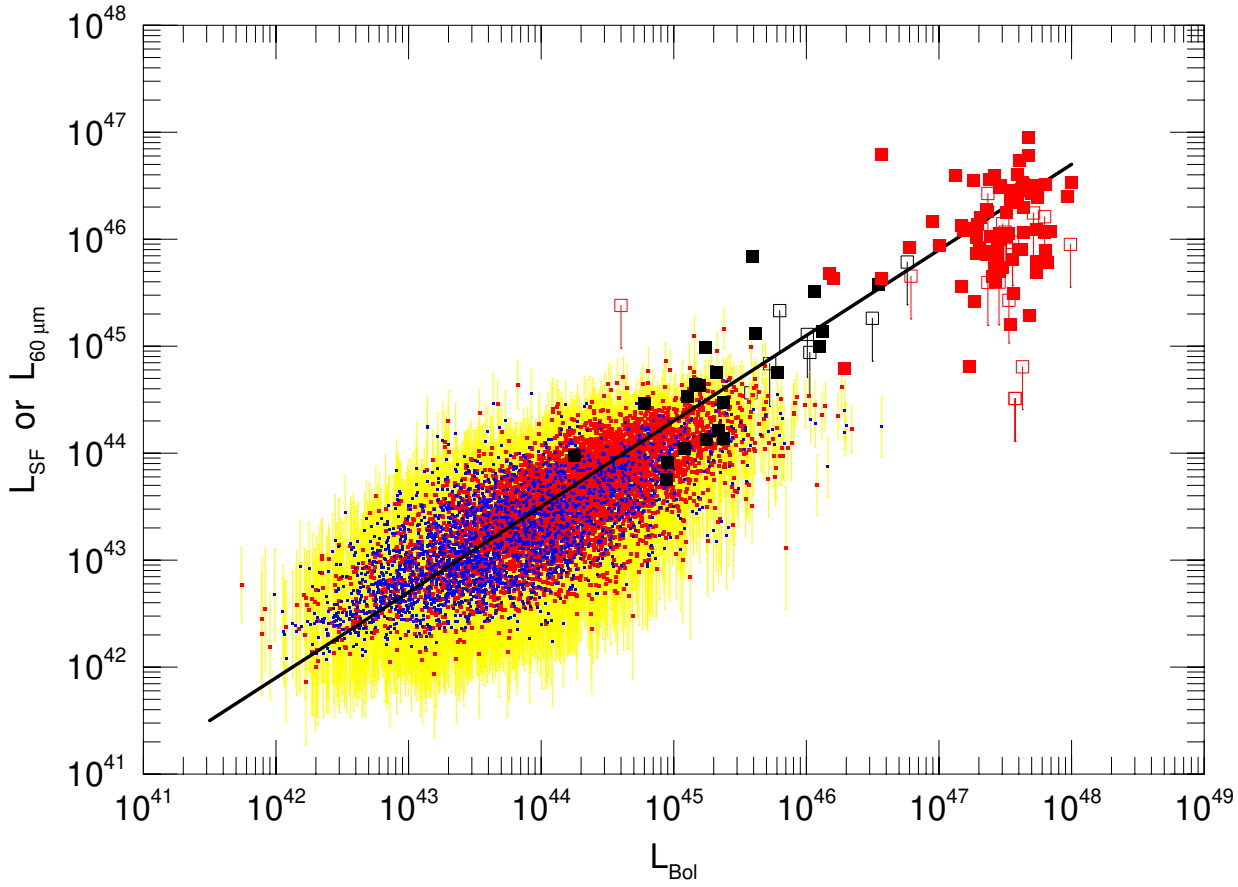

Figure 1.3: From Netzer (2009). $L_{\rm SF}$ vs. $L_{\rm bol}$ for AGN. The type-II AGN from Kewley et al. (2006) are the small points with yellow error bars. The red points are Seyfert 2s and the blue points are type-II LINERs. QUEST QSOs from Netzer et al. (2007) are shown as large black squares and high redshift QSOs from Lutz et al. (2008) as large red squares. Empty symbols with lines represent upper limits. The slope of the straight line is 0.8.

Chapter 2

ALMA Observations and Data Analysis

2.1 Sample and Campaign Background

Our original sample is a selection of the 38 brightest ($L_{\rm bol} \sim 3-23\times10^{46}$ erg s^{-1}) unobscured quasars from the sixth data release of the Sloan Digital Sky Survey (SDSS/DR6; York et al., 2000; Adelman-McCarthy et al., 2008) at redshifts z $\sim 4.65-4.92$. This redshift range, which we will often refer to as $z \simeq 4.8$, was selected to allow follow up observations of the Mg II λ2798 emission line and nearby 3000 Å continuum luminosity. Observations of Mg II were carried out using VLT/SINFONI and Gemini-North/NIRI and presented in Trakhtenbrot et al. 2011, T11 hereafter, which provided estimates of the SMBH masses (M_{BH}) and accretion rates of the quasars ($L/L_{\rm Edd}$). These results indicated that the sample, on average, has higher accretion rates ($L/L_{\rm Edd} \sim 0.6$) and lower SMBH masses ($\sim 8.4\times10^8 M_\odot$) than AGN observed at lower redshifts.

Further observations were carried out with the *Herschel* Spectral and Photometric Imaging Receiver (SPIRE) (Mor et al., 2012; Netzer et al., 2014, M12 and N14 henceforth), and relied on data from the *Spitzer* Infrared Array Camera (IRAC) (also from N14) 3.6 and 4.5 μm bands for positional priors for the *Herschel* photometry. While the majority of sources were detected using Spitzer, only nine source were detected in all three SPIRE bands. We define these *Herschel*/SPIRE detections as "FIR-bright" sources, having on average $L_{FIR} \sim 8.5\times10^{46}\,{\rm erg\,s^{-1}}$ ($2.2\times10^{13}L_\odot$). By using the standard conversion factor based on the IMF of Chabrier (2003) we calculated star formation rates as $SFR/M_\odot\,{\rm yr^{-1}} = L_{FIR}\,/10^{10}L_\odot$, giving SFRs $\sim 1000-4000\ M_\odot\,{\rm yr^{-1}}$ for our nine FIR-bright sources. To determine the SFRs of the *Herschel* non-detected sources, which we refer to as "FIR-faint" sources, stacking analysis was carried out in Netzer et al. (2014) and gave a median SFR of $\sim 400\ M_\odot\,{\rm yr^{-1}}$. The work of N14 and M12 indicate that there is a wide variation of SFRs in our sample, while we see in T11 that the variation of SMBH and AGN properties are more uniform across the sample.

The goal of the *Herschel*/SPIRE campaign was to determine the peak of the SF heated dust continuum (M12, N14), and if possible, to observe evidence for merger activity. However,

the size of the field of view and the spatial resolution of the data ($\sim 18''$, or $\gtrsim 100\,\mathrm{kpc}$ at $z \simeq 4.8$) was insufficient to determine the presence of close nearby systems.

2.2 ALMA Observations

Our sample of objects were observed in two projects in ALMA band-7. The first project observed six objects in total, three FIR-bright and three FIR-faint sources, and was a part of cycle-2 (project code 2013.1.01153.S) during the period 2014 July 18 to 2015 June 13. The second project observed twelve additional objects, six FIR-bright and six FIR-faint sources, and was a part of the cycle-4 (project code 2016.1.01515.S) for the period of 2016 November 9 to 2017 May 6. The cycle-2 observations were published in Trakhtenbrot et al. (2017) while the cycle-4 data has been submitted as Nguyen et al. (2020).

The cycle-2 observations where carried out with the extended C34-4 configuration, while the cycle-4 observations used the C40-5 configuration. Because the ALMA observatory was expanded between observations the number of 12-m antennas varied, but we strove to obtain the same angular and spatial resolution. The exposure time ranged from 1001 - 2276 seconds, with an observed angular resolution variation of 0.19-0.33″ and a central frequency range of 317 - 349 GHZ. The observed angular resolution corresponds to ~ 2 kpc at $z \simeq 4.8$. We chose the TDM correlator mode which provides four spectral windows, each covering an effective bandwidth of 1875 MHz, which corresponds to $\sim 1650\,\mathrm{km\,s^{-1}}$ at the observed frequencies. This spectral range is sampled by 128 channels with a frequency of 15.625 MHz or $\sim 15\,\mathrm{km\,s^{-1}}$ per channel. The default spectral resolution of ALMA is given as roughly twice the size of the channels, i.e. $\sim 30\,\mathrm{km\,s^{-1}}$. Two such spectral windows were centered on the frequency corresponding to the expected peak of the [C II] line, estimated from the Mg II-based redshifts of our targets (as determined in T11).

Because of the specific redshifts of the sources, the spectral windows were found to be affected by poor atmosphere transmission, and due to variation between observations we note that our cycle-4 data was more affected, resulting in noisier [C II] data. The other two adjacent spectral windows were placed at higher frequencies and separated from the first pair by about 12 GHz. Each of these pairs of spectral windows overlapped by roughly 50 MHz. However, the rejection of a few channels at the edge of the windows due to divergent flux values (a common flagging procedure in ALMA data reduction), leads to a small spectral gap between pairs of windows. This presents some issues for certain targets (Section 2.2.1). Given this spectral setup of four bands, the ALMA observations could in principle probe [C II] line emission over a spectral region corresponding to roughly $\sim 3000\,\mathrm{km\,s^{-1}}$ ($\Delta z \simeq 0.06$). Table 2.1 is an observation log with additional details of the ALMA observations. We will use abbreviated object names (i.e., "JHHMM") in the rest of this thesis.

2.2.1 Data Reduction

Data reduction was performed using the CASA package version 4.5.0 and 4.7.2 (McMullin et al., 2007). `CLEAN` algorithms were ran with "briggs" weighting and a robustness parameter of 0.5 in order to create continuum and emission line images. Continuum emission images were constructed using the line-free spectral window pair, while the `UVCONTSUB` command was used to subtract continuum emission from the [C II] window pair, resulting in continuum-

Table 2.1: Observation Log

sub-sample	Target ID	$N_{\rm Ant}$†	$T_{\rm exp}$ [sec]	F_ν rms [mJy/beam]	Beam size [″]	Pixel Size [″]	ALMA Companions
Bright	SDSS J033119.67r074143.1 T17	29	792	9.2×10^{-2}	0.41×0.31	0.06	...
	SDSS J080715.11+132805.1 N20	43	2054	5.1×10^{-2}	0.37×0.21	0.06	...
	SDSS J134134.20+014157.7 T17	35	697	5.6×10^{-2}	0.38×0.30	0.06	...
	SDSS J140404.63+031403.9 N20	42	1184	6.2×10^{-2}	0.36×0.29	0.06	...
	SDSS J143352.21+022713.9 N20	40	1001	5.1×10^{-2}	0.37×0.32	0.06	...
	SDSS J151155.98+040803.0 T17	30	729	8.7×10^{-2}	0.53×0.31	0.06	SMG (w/ [C II]), "B" (w/o [C II])
	SDSS J161622.10+050127.7 N20	43	1690	3.6×10^{-2}	0.23×0.19	0.06	...
	SDSS J165436.85+222733.7 N20	42	1305	5.5×10^{-2}	0.27×0.21	0.06	...
	SDSS J222509.19−001406.9 N20	40	1486	5.4×10^{-2}	0.29×0.23	0.06	...
Faint	SDSS J092303.53+024739.5 T17	38	2978	4.3×10^{-2}	0.51×0.29	0.06	SMG (w/ [C II])
	SDSS J093508.49+080114.5 T17	33	3230	5.1×10^{-2}	0.54×0.29	0.06	...
	SDSS J101759.63+032739.9 N20	41	2064	2.8×10^{-2}	0.36×0.24	0.06	...
	SDSS J115158.25+030341.7 N20	42	1851	5.1×10^{-2}	0.33×0.28	0.06	...
	SDSS J132110.81+003821.7 N20	40	2276	2.8×10^{-2}	0.33×0.30	0.06	...
	SDSS J132853.66−022441.6 T17	36	2852	4.2×10^{-2}	0.48×0.31	0.06	SMG (w/ [C II])
	SDSS J144734.09+102513.1 N20	39	1871	5.1×10^{-2}	0.54×0.31	0.06	SMG (w/ [C II])
	SDSS J205724.14−003018.7 N20	39	1550	4.4×10^{-2}	0.28×0.21	0.06	SMG (w/ [C II]), "B" (w/o [C II])
	SDSS J224453.06+134631.6 N20	40	1881	3.4×10^{-2}	0.32×0.29	0.06	...

† Number of ALMA antennas used.
T17 Cycle-2 data originally published in Trakhtenbrot et al. (2017)
N20 Cycle-4 data used in Nguyen et al. (2020)

subtracted cubes. Observed flux densities and beam deconvolved continuum source sizes are presented in Table 4.1.

Sizes of the continuum emitting regions were determined from the respective images by fitting spatial 2D Gaussians to the sources, which are characterized by a peak flux, semi-major and semi-minor axes, and a position angle. The fluxes were measured by integrating over these spatial 2D Gaussians. The SMG companion to J2057 (see Section 2.2.2), however, seems to be composed of two separate sources which were not properly fitted by the CASA 2D Gaussian routine. Instead, sizes were obtained directly from the continuum images using an azimuthally averaged Gaussian fit. Since these values are not beam-corrected, they are quoted as upper limits in Table 4.1.

Various `IMMOMENTS` commands gave the velocity fields and velocity dispersion maps (first and second moment, respectively) from the [C II] continuum subtracted cubes. To measure the properties of the [C II] emission lines, we used both a "spatial" and "spectral" method. In the "spatial" approach, we created zero-moment images (i.e., integrated over the spectral axis) for all sources and fitted the spatial distribution of line emission with 2D Gaussian profiles. Line fluxes were obtained as described before for the continuum flux determinations. In the "spectral" approach, we extracted 1D spectra from the [C II] continuum subtracted cubes. A Gaussian profile was fitted to the emission line profiles, from which we obtained the integrated line flux.

We found that both methods measured the [C II] line fluxes with a median difference of 0.05 dex. Ultimately, we used the "spatial" approach for the majority of our objects because it is less sensitive to the low Signal-to-Noise (S/N) outer regions of the sources and the low S/N edges of the line profiles. J2057, however, has a spectral gap (as described in 2.2) lying in the center of the [C II] line. This proved difficult for the "spatial" method as no interpolation of the missing line flux was possible. Hence, the line flux reported in Table 4.1 was obtained with the "spectral" approach. Also, both SMG companions to J1447 and J2057 (see next

section) show separate dynamical components. In the case of J1447 the "spectral" approach was used to determine their properties. The J2057 SMG also breaks into two components in continuum emission, which are not clearly related to the [C II] emission. Both components are characterized in Table 4.1, with more detail in the next section.

2.2.2 Source Detection

We detect sixteen of our eighteen quasars clearly in both continuum and [C II] emission with 6-12σ significance. While J1447 is only detected at a 3σ level in [C II] line, and J1151 is not detected at all. J1447 and J1151 are both FIR-faint sources. Because J1447 has a very weak signal, it was not possible to fit a Gaussian to the spatial distribution of its line and continuum emission. Instead, 'aperture' photometry was carried out with an area corresponding to roughly the beam size. The [C II] emission of J1447 was found to have a S/N $\sim$ 3.6, while there was a non-significant signal in the continuum. The continuum values listed in Table 4.1 for J1447 and J1151 correspond to 3 times the average RMS noise about the expected quasar positions.

Four FIR-faint quasars (J0923, J1328, J1447 and J2057) and one FIR-bright quasar (J1511) show the presence of nearby sub-mm emitting sources. Because these nearby sources are detected in both continuum and [C II] emission with a significance of 6-9 σ, these are our expected companions. Continuum maps for these sources are presented in Figure 2.1, while the measurements of these SMGs are also listed in Table 4.1. The SMGs are separated from the QSO by 14 - 59 kpc and have a median continuum flux density of 1.2 mJy. It should be noted that the peak of the SMG [C II] lines are offset from the peak of the QSO [C II] lines by $< 450 \mathrm{km\,s^{-1}}$, these clearly associated lines further reinforce that these SMGs are nearby, interacting companions. Both J2057 and J1511 have a source of nearby emission detected only in the continuum which are marked by with a 'B' in Figure 2.1, and are separated from their respective quasars by $6\farcs3$ and $3\farcs9$. When accounting for the redshifts of these QSOs, the continuum only source of J2057 is separated by 41.8 kpc while for J1511 the separation is 25 kpc. Both of these continuum only sources are further from the QSO than the additionally detected SMGs for J1511 and J2057. Despite having a lower limit of $\pm$1500 $\mathrm{km\,s^{-1}}$ to the velocity shift of the [C II] emission from the quasar host, we do not detect any [C II] lines in these continuum only sources. Because of the separation and lack of a [C II] line detection, we conclude that this continuum sources are most likely a source only seen in projection.

For all our quasars detected in both, continuum and [C II], the two emissions follow each other well. The exceptions are the two detected SMGs of our Cycle 4 data; J2057 and J1447. Their detailed continuum and [C II] maps are presented in Figure 2.1. In the case of J1447, the continuum emission seems more extended towards the north than the [C II] emission, although weaker, redshifted [C II] emission appears towards the north in dynamical maps (see next Section). The SMG to J2057 has secondary peaks in [C II] and continuum emission. These are labeled as E, W and NE, SW in Figure 2.1, respectively. We will see in the next Chapter that there is strong indication of gravitational perturbations in these two SMG sources.

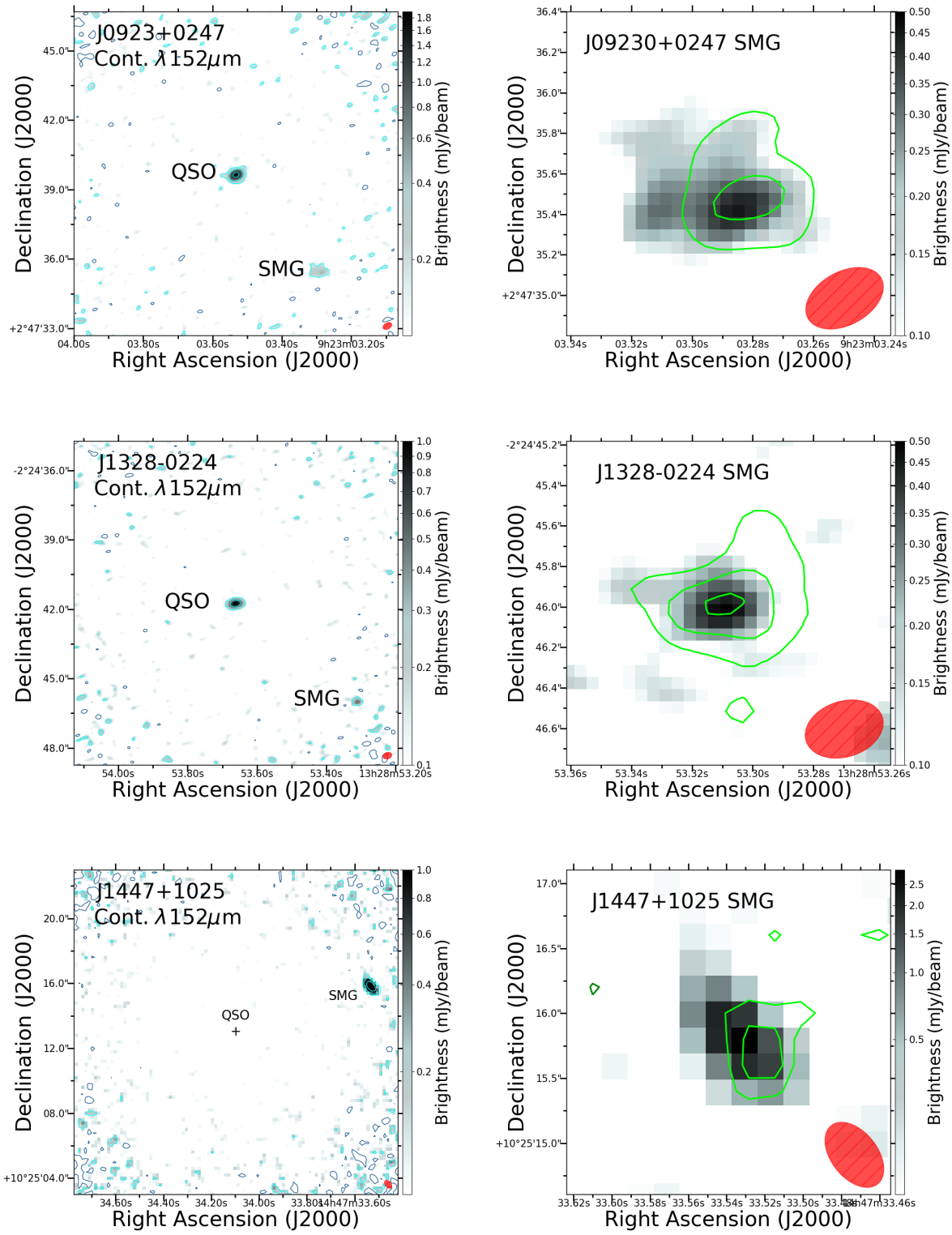

Figure 2.1
(Continued on the next page.)

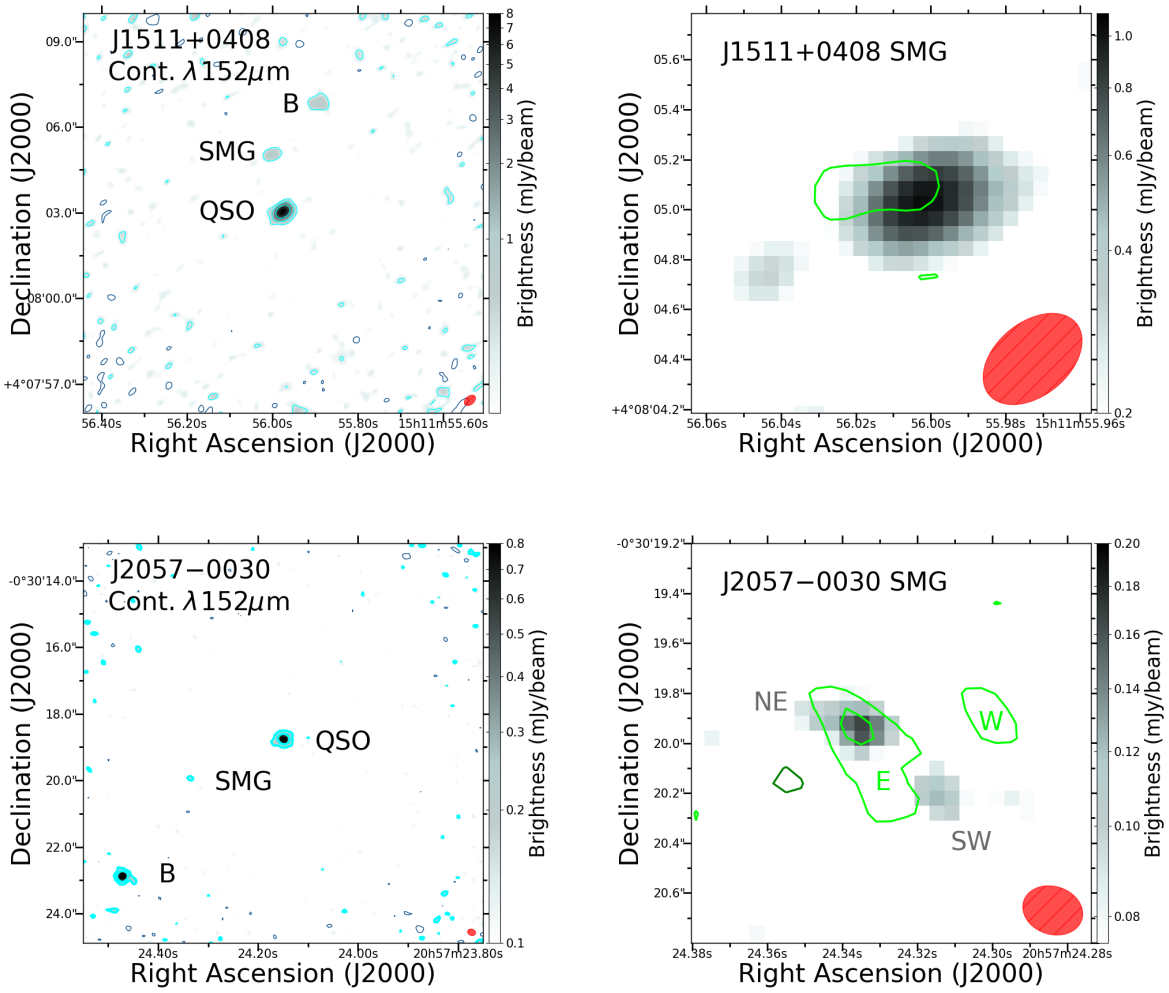

Figure 2.1: The **Left column** is large-scale continuum images for our sample where companions have been found. Note that J1447 is *not* detected in dust continuum. The gray-scale maps show the continuum emission determined from the line-free ALMA spectral windows. Cyan and blue contours trace emission levels at different positive and negative significance levels, respectively, with the first contour tracing the region where the continuum emission exceeds 2σ, and consecutive contours plotted in steps of 2σ. Physical companions, i.e., sources that have clear [C II] detections with redshifts consistent with those of the quasars, are marked as "SMG". The continuum sources accompanying J1511 and J2057 that lack significant [C II] emission are marked as "B". The **Right column** is small-scale continuum and [C II] line emission maps derived for the accompanying SMGs of our sample. For each source, the gray-scale map traces the continuum emission, while the light green contours trace the [C II] line emission (i.e., surface brightness) at significance levels of 3 and 6-σ. For each source, the line fluxes used for the contours were extracted from a spectral window spanning $\pm 500\,\mathrm{km\,s^{-1}}$ around the [C II] line peak. The two J2057 components observed in [C II] emission are labeled E and W, while the two components seen in continuum are labeled NE and SW. For both columns of images the ALMA beams are shown as red ellipses near the bottom-right of each panel.

2.3 Companions at High Redshift

Before moving on to the analysis and discussion of the host characteristics of our sample, we would like to take a moment to stress the significance of our companion detections.

Current cosmological models recognize high-z quasars as sign-posts of high-density environments (see Costa et al. 2014 and references therein). It is therefore not unexpected that our sample shows a larger number of companions when compared to ALMA observations of blank fields. Recent blank deep field surveys conducted with ALMA (Carniani et al., 2015; Aravena et al., 2016a; Fujimoto et al., 2016) imply that each ALMA pointing of 18″ should have of the order of ~ 0.1 SMGs at a flux limit of 15 μJy at 1.2mm. Other measurements of the HST Legacy Fields (Bouwens et al., 2015) and the Great Observatories Origins Deep Survey (GOODS) Fields (Stark et al., 2009) give surface densities on the order of 0.01 galaxies per single ALMA band-7 pointing (for SMGS with SFR $\sim 100\,M_{\odot}\,\mathrm{yr}^{-1}$). Though they have not been confirmed with higher S/N, Aravena et al. (2016b) cites a number count of roughly 0.06 [C II]-emitting $z \sim 5-8$ galaxies per ALMA pointing of the Hubble Ultra Deep Field.

As quasars, SMGs are also highly clustered and seem to be hosted by massive dark matter halos (Wilkinson et al., 2017). Several works have found a significant portion of sub-mm sources with multiple components, 35 to 80 percent depending on the resolution and flux limit (Hodge et al., 2013; Bussmann et al., 2015; Scudder et al., 2016; Hayward et al., 2018).

In a recent study of multiplicity of far-infrared bright quasars, Hatziminaoglou et al. (2018) assembled a random sample of 28 infrared-bright SDSS quasars with detections in *Herschel*/SPIRE. This sample of detected quasars would correspond to our FIR-bright objects in terms of L_{AGN}, M_{BH}, and Eddington ratios, but with $z \sim 2-4$. Using the ALMA Atacama Compact Array (ACA) Hatziminaoglou et al. (2018) found that 30 percent of their targets were found to be multiple. However ACA does not provide the same depth or resolution as our observations, and the redshift of these sub-mm sources were not confirmed.

Decarli et al. (2017, 2018) present a similar study of [C II] and dust continuum at a similar redshift to our study, where the ALMA observations provide enough information to indicate whether the nearby sources are real companions. They found that 4/25 rapidly star-forming galaxies have a companion, i.e., 16 percent. Based on the IR-luminosities reported by Decarli et al. (2018), 20 quasars hosts would be classified as FIR-faint for a threshold FIR luminosity of $10^{12.9}$ $L_{\odot}$, and 3/4 of the companions would be associated to FIR-faint quasar hosts.

Our total observed sample of 18 quasars has 5 sources with companions, 1 FIR-bright (J1511) and 4 FIR-faint (J0923, J1328, J2057, and J1447), i.e., 28 percent. J0923 and J1328 have no nearby sources in *Spitzer*/IRAC, while J2057 and J1447 were not observed by *Spitzer*. J1511 has two further nearby *Spitzer*/IRAC sources. It is interesting that we only find that 1 FIR-bright target is multiple in ALMA observations, a rate much lower than that found in the randomly selected FIR-bright sample of Hatziminaoglou et al. (2018), and that we find a percentage of companions slightly higher than that reported by Decarli et al. (2017).

Table 2.2: Spectral Measurements

Subsample	Target		Cont. Flux	ν	Cont. Size	$F_{[\mathrm{C\,II}]}$	$\mathrm{FWHM}_{[\mathrm{C\,II}]}$	$\nu_{0,[\mathrm{C\,II}]}$	[C II] size	$L_{[\mathrm{C\,II}]}$	Δd	Δv
	ID	comp.	[mJy]	[GHz]	[″]	[Jy km s^{-1}]	[km s^{-1}]	[GHz]	″	[$10^9\,L_\odot$]	[kpc]	[km s^{-1}]
Bright	J0331	QSO	4.3 ± 0.2	344.47	0.18×0.11	5.2 ± 0.5	495 ± 31	331.29 ± 0.006	0.25×0.15	3.58	...	...
	J0807	QSO	6.80 ± 0.20	334.87	0.23×0.19	5.8 ± 1.40	398.6 ± 19.2	323.27 ± 0.010	0.52×0.14	4.01	. . .	. . .
	J1404	QSO	11.31 ± 0.27	333.86	0.28×0.25	5.81 ± 0.71	483.3 ± 21.3	320.86 ± 0.009	0.52×0.43	4.08	. . .	. . .
	J1433	QSO	7.61 ± 0.33	334.05	0.32×0.26	4.79 ± 0.38	397.0 ± 13.7	331.78 ± 0.006	0.43×0.37	3.17	. . .	. . .
	J1341	QSO	18.5 ± 0.5	346.84	0.23×0.21	6.1 ± 0.8	384 ± 16	333.41 ± 0.006	0.47×0.28	4.51	...	...
	J1511	QSO	10.4 ± 0.3	347.99	0.22×0.19	5.3 ± 0.4	507 ± 36	334.69 ± 0.011	$< 0.39 \times 0.12$	3.42	...	...
	J1511	SMG	1.6 ± 0.2	347.99	0.43×0.11	2.4 ± 0.7	313 ± 38	334.61 ± 0.021	$< 0.94 \times 0.16$	1.53	13.9	+75
	J1616	QSO	6.29 ± 0.28	335.74	0.23×0.16	10.1 ± 1.50	469.5 ± 24.1	322.99 ± 0.011	0.60×0.36	7.00	. . .	. . .
	J1654	QSO	4.73 ± 0.10	344.53	0.10×0.08	2.07 ± 0.46	543.0 ± 34.9	331.81 ± 0.016	0.31×0.08	1.36	. . .	. . .
	J2225	QSO	13.13 ± 0.21	334.61	0.22×0.17	8.05 ± 0.73	445.5 ± 22.4	322.50 ± 0.010	0.44×0.29	5.60	. . .	. . .
Faint	J0923	QSO	3.0 ± 0.1	348.65	0.28×0.24	4.1 ± 0.3	363 ± 11	336.09 ± 0.005	0.45×0.34	3.21	...	...
	J0923	SMG	1.2 ± 0.3	348.65	0.57×0.36	4.1 ± 0.7	214 ± 10	335.82 ± 0.004	0.60×0.31	2.16	36.5	+246
	J0935	QSO	1.6 ± 0.1	347.93	0.26×0.16	0.9 ± 0.2	338 ± 42	334.49 ± 0.016	0.44×0.25	0.80	...	...
	J1017	QSO	1.36 ± 0.10	331.76	0.23×0.20	1.93 ± 0.27	223.8 ± 8.3	319.49 ± 0.004	0.32×0.30	1.37	. . .	. . .
	J1151[a]	QSO	< 0.81	346.13	. . .	< 0.31	. . .	. . .	. . .	. . .	. . .	. . .
	J1321	QSO	1.56 ± 0.07	343.73	0.29×0.22	1.72 ± 0.21	480.7 ± 26.4	322.12 ± 0.012	0.46×0.27	1.13	. . .	. . .
	J1328	QSO	1.7 ± 0.1	348.74	0.40×0.21	3.1 ± 0.3	221 ± 14	336.59 ± 0.008	0.35×0.31	1.63	...	...
	J1328	SMG	0.7 ± 0.2	348.74	$< 0.56 \times 0.26$	2.0 ± 0.3	423 ± 43	337.07 ± 0.020	0.71×0.44	2.01	44.5	−432
	J1447	QSO[b]	< 0.12	346.61	. . .	0.18 ± 0.06	293.2 ± 113.6	334.50 ± 0.027	0.30×0.28	0.14	. . .	. . .
	J1447	SMG[c]	3.86 ± 0.17	346.61	0.40×0.15	0.88 ± 0.27	215 ± 22	334.37 ± 0.008	< 0.3	0.57	59	206.5
	J1447	SMG[c]				0.54 ± 0.16	199 ± 33	333.72 ± 0.008	< 0.3	0.35	59	701.2
	J2057	QSO	2.03 ± 0.14	346.52	0.24×0.21	2.51 ± 0.31	331.4 ± 20.5	334.44 ± 0.009	0.40×0.18	1.63	. . .	. . .
	J2057	SMG[d]NE,E	0.28 ± 0.04	346.52	< 0.3	0.63 ± 0.11	475.4 ± 84	334.62 ± 0.009	< 0.3	0.41	20	-161.4
	J2057	SMG[d]SW,W	0.17 ± 0.06	346.52	< 0.3	0.37 ± 0.07	336.3 ± 68	334.32 ± 0.009	0.57×0.14	0.24	20	107.7
	J2244	QSO	3.34 ± 0.09	346.95	0.20×0.19	3.86 ± 0.29	283.1 ± 7.4	335.71 ± 0.003	0.40×0.30	2.49	. . .	. . .

[a] 3-σ upper limit of the calculated RMS at the expected position of the source.

[b] Line fluxes were determined by aperture photometry at the position of the source.

[c] Two Gaussian profiles were fitted to the [C II] line spectra. Source sizes have upper limits only.

[d] Two components are seen in continuum (NE and SW) and [C II] (E and W). Most source sizes have upper limits only.

Chapter 3

Line and Dust Emission properties

3.1 Emission Line Velocity Offsets

Because neutral carbon has a low ionization potential (11.3 eV) and can be excited by electron collisions, [C II] emission can be found in neutral ISM throughout a galaxy particularly tracing photo-dissociation regions, that is, naturally diffuse and partially ionized gas. Although from observations in the local universe it is seen that the [C II] line is broader than molecular gas (e.g., Goicoechea et al. 2015), because of its high brightness and narrow intrinsic width it is a good measure of the systemic redshift of the quasar host galaxy. While the Mg II line, produced in the vicinity of SMBHs in the so called Broad Line Region (BLR), is dominated by the gravitational force of the SMBH as well as other central bulk nuclear winds or turbulences and is therefore a better tracer of the redshift of the quasar itself. In Table 3.1 we compare the redshifts obtained from the [C II] and Mg II lines ($\Delta v_{\rm Mg\,II}$) for our 17 quasar hosts with detected [C II]. While [C II] is a good tracer of ionized gas throughout a galaxy and should coincide with the systemic redshift of our quasar hosts, the Mg II line is produced in the vicinity of the super massive black holes, in the so called Broad Line Region (BLR). For unobscured AGN at moderate redshifts ($z < 2$), the BLR Mg II line is found within ~ 200 km s^{-1} of the systemic redshifts (Richards et al., 2002; Shen et al., 2016; Mejía-Restrepo et al., 2016). The large dispersions in the line shifts are clearly due to the broad nature of the BLR lines and hence the difficulties in determining precise line centers.

For comparison, we also list the SDSS-based redshift determinations published in Hewett & Wild (2010), along with the difference with respect to the [C II] line (Δv_{SDSS}). At $z \sim 5$ SDSS-based redshifts would be determined using the BLR UV Lyα, S IV and C IV emission lines, which are usually considered problematic because of the absorbed Lyα profile, the weakness of the S IV line, and the well established blueshifts present in the C IV line. In fact, we see no correlation between Δv_{SDSS} and $\Delta v_{\rm Mg\,II}$, most likely because of the uncertainties associated to the z_{SDSS} determinations (Mason et al., 2017).

From Table 3.1 we can see that most objects in our total sample of 17 quasar hosts have significant blueshifts of the Mg II line with respect to the [C II] line ($\Delta v_{\rm Mg\,II} > 0$). The average value for $\Delta v_{\rm Mg\,II}$ is 464 km s^{-1}, with a standard deviation of 657 km s^{-1}. As Venemans et al. (2016) already pointed out, since the distribution of offsets in not centered around 0 km s^{-1},

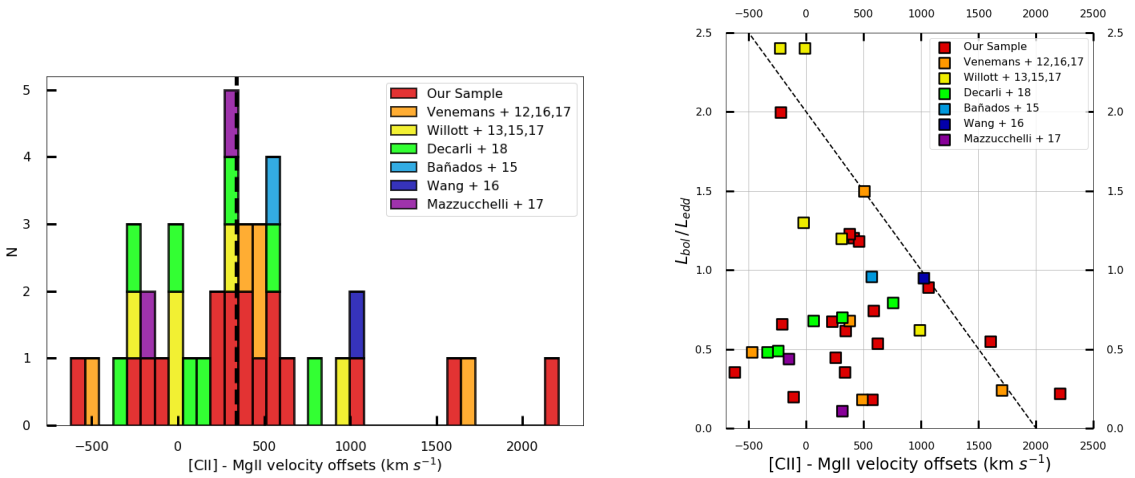

Figure 3.1: **Left:** Histogram presenting the distribution of the velocity shifts of the Mg II with respect to the [C II] emission lines of the quasars. Our observations are at $z \simeq 4.8$, while those in Venemans et al. (2016), Willott et al. (2013, 2015, 2017) etc. are at $z \gtrsim 6$. The [C II] line is clearly redshifted with respect to the Mg II measurements with a mean and standard deviation of 372 ± 582 km s^{-1}. The vertical line denotes the median of 337 km s^{-1}. **Right:** Eddington ratios of our compiled quasars against the observed Mg II offsets. References for the Mg II measurements and the Eddington ratios can be found in Table 3.2. The average Eddington Ratio is 0.83. 37 quasars are plotted in total. Only 5 of the 8 Decarli quasars have published Eddington ratios.

we can assume that they are not due to the uncertainty associated with fitting the broad emission line of Mg II. This is further supported by Shen et al. (2016), where they state that the intrinsic uncertainty of using the Mg II broad-line for estimating redshifts is 200 km s^{-1}, smaller than our median offset. We find no noticeable correlation between Mg II offsets and the presence of companions.

Venemans et al. (2016) compiled a list of $z > 6$ quasars and compared the redshift measurements from the Mg II line and those of the CO molecular line or the [C II] atomic line. The median of the $z_{\rm [C\,II]/CO} - z_{\rm Mg\,II}$ distribution for their sample is 467 km s^{-1} with a standard deviation of 630 km s^{-1}, almost identical to our findings. We created our own compilation, but used exclusively quasars with a measured [C II] line for the sake of congruity. The compilation is populated by our total sample of 17 quasars, eight quasars taken from Decarli et al. (2018), five quasars found in Willott et al. (2013, 2015, 2017), five quasars from Venemans et al. (2012, 2016, 2017), two from Mazzucchelli et al. (2017), and one each from Banados et al. (2015) and Wang et al. (2016). We present the Mg II offsets of this compilation as a histogram in Figure 3.1 and in Table 3.2. For this compilation we found a mean $z_{\rm [C\,II]} - z_{\rm Mg\,II}$ of 372 km s^{-1}, a median of 337 km s^{-1}, and a standard deviation of 582 km s^{-1}. It should be noted that only our sample is at $z \simeq 5$, while the quasars from the literature are all at $z \gtrsim 6$. The mean and median of the $z \gtrsim 6$ only quasars are 300 and 309 km s^{-1}, respectively, very close to the results from our full compilation. This result strongly suggests a velocity difference between the BLR and quasar host galaxies of several hundred km s^{-1}.

Blueshifts are usually associated to outflowing gas which is approaching the observer.

Table 3.1: Redshifts and [C II] Line Shifts

Sub-sample	Target	$z_{[\mathrm{C\,II}]}$	z_{SDSS}	Δv_{SDSS} km s^{-1}	$z_{\mathrm{Mg\,II}}$[a]	$\Delta v_{\mathrm{Mg\,II}}$ km s^{-1}
Bright	J0331	4.737	4.732	+257	4.729	+412
	J1341	4.700	4.682	+981	4.689	+573
	J1511	4.679	4.677	+88	4.670	+456
	J0807	4.879	4.871	+378	4.874	+256
	J1404	4.923	4.871	+2208	4.880	+2208
	J1433	4.728	4.685	+2281	4.721	+379
	J1616	4.884	4.863	+1061	4.872	+620
	J1654	4.728	4.707	+1081	4.730	−112
	J2225	4.716	4.883	+508	4.886	+340
Faint	J0923	4.655	4.650	+257	4.659	−213
	J0935	4.682	4.699	−911	4.671	+588
	J1017	4.949	4.918	+1559	4.917	+1605
	J1151	—	4.699	—	4.698	—
	J1321	4.722	4.739	−882	4.716	+337
	J1328	4.646	4.650	−188	4.658	−621
	J1447	4.682	4.688	−329	4.686	−224
	J2057	4.683	4.685	−97	4.663	+1064
	J2244	4.661	4.621	+2153	4.657	+225

[a] Mg II λ2798-based redshifts taken from T11.

Blueshifts seen in the C IV line, for example, are usually interpreted as evidence for nuclear outflows and they seem to correlate well with accretion rate (Coatman et al., 2016; Sulentic et al., 2017; Vietri et al., 2018; Sun et al., 2018; Ge et al., 2019). We have looked for such correlation for the objects in our compilation and found none. Figure 3.1 presents the accretion rate in units of Eddington (as reported in the literature) versus the measured [C II]-Mg II shifts. A rather low correlation coefficient is determined, with $r = -0.23$, with the probability of an uncorrelated system $p = 0.17$. In fact, Figure 3.1 suggests that low accretion sources can show a wide range of possible shifts, while high-Eddington sources tend to show a smaller range of offsets, if any. However, this could be a bias due to the scarcity of super-Eddington sources among quasars (Pognan et al., 2020; Wyithe & Loeb, 2012). We also tested a correlation of the offsets with infrared luminosities (compiled values can also be found in Table 3.2) but no significant result was found ($r = 0.26$, $p = 0.12$).

We find no correlation with high offsets and the presence of companions. On average the mean offset of objects with companions is lower than the entire sample (92.4 km s^{-1}). Interestingly, of the four quasars with companions presented in Decarli et al. (2018), two have tabulated [C II]-Mg II offsets in Table 6, giving a mean offset of ~ 0 km s^{-1}. Since the number of sources with companions is very small, these are by no means conclusive findings, but suggest a possible link between merger activity and smaller [C II]-Mg II shifts.

3.2 [C II] Line Spectrum and Host Velocity

In Figure 3.2, we plot the continuum subtracted [C II] spectral region for all 18 quasar hosts presented in this work, including J1151 which was undetected in both continuum and [C II], and J1447 which had a 3σ level detection in [C II]. We also include spectra for all five accompanying SMGs. A best-fit line model using a Gaussian profile is overlaid. The Root Mean Square (RMS) spectra is plotted below each emission line spectra.

From the ALMA data cube spectrum, we are able to compute the moments of the Line of Sight Velocity Distribution (LOSVD). Figure 3.3 shows moment 1 velocity maps for the sixteen quasar hosts significantly detected in [C II] and the five companion SMGs. The weak [C II] emission from J1447 was not sufficient to determine moment maps.

For all our objects only half have well behaved velocity maps, with a clear velocity gradient across the system, which suggests rotation of a flat gaseous structure. The remaining sources show noisier, more irregular maps although evidence for a velocity gradient is still present. We find that the morphologies of our FIR-Bright quasars mostly show uniform, rotation dominated maps (7/9). While the FIR-faint objects show weaker velocity gradients and disrupted morphologies, with only 3/7 objects with a strong rotation signature. This is possibly due to some of our sources being observed through spectral sub-mm windows with worse transmission, as mentioned in Section 2.2.

Some of our quasar hosts show increased velocity dispersions in the centers of the [C II] - emitting regions, with $\sigma_v \sim 100$ km s^{-1}, which can be an indication of beam smearing. This could lead us to overestimate the rotation kinematics we see in Figure 3.3. However we do not expand on correcting this smearing as other studies of sub-mm sources have done, as our targets are only partially resolved and modeling the rotation is not possible. In fact, as many of our sources do not exhibit clear rotation dominated kinematics (e.g., J1017 and J1654), other factors could be affecting the kinematics of our hosts. Possible alternatives such as a turbulent component have been demonstrated in several recent studies of resolved ISM kinematics in high-redshift galaxies (e.g., Gnerucci et al., 2011; Williams et al., 2014; Díaz-Santos et al., 2016).

The majority of our objects have a single peak line profile except for J1404 which exhibits double peak emission in the [C II] line, and the SMG companion to J1447. The double feature seen in J1404 has two peaks separated ~ 350 km s^{-1} from each other, while the SMG of J1447 shows two components to the [C II] line separated by ~ 600 km s^{-1}. The velocity map of J1404 in Figure 3.3 shows a single source with strong rotational signatures and a large total velocity amplitude of ~ 400 km s^{-1}, roughly the same separation we see in the spectrum. Therefore, this double peak emission is most likely due to the rotation dominated morphology of the host galaxy.

On the other hand, the double feature seen in the SMG of J1447 most likely corresponds to a double source. This is seen in the bottom right panel of Figure 3.3 where two spatially separated kinematic components appear. The north-east peak is rather weak, as it is below the 3σ threshold of the [C II] contours, but it is clearly recovered in the spectrum shown in Figure 3.2 and coincides with strong emission seen in dust continuum (see Figure 2.1).

Finally, J2057 also presents some interesting dynamical features. Besides the presence of two dust continuum peaks and a complex velocity map shown by the companion SMG, the quasar itself shows strong evidence for dynamical disruption: its [C II] emission appears as consistent with a ~ 100 km s^{-1} rotating disk plus debris material and a ~ 20 kpc-long collimated 'tadpole-like' structure orientated roughly in the E-W direction, which is constrained to a very narrow velocity range. This structure is not apparent in Figure 3.3 because of the velocity binning. J2057 and its SMG companion will be the subject of a future work.

FIR-Bright Objs.

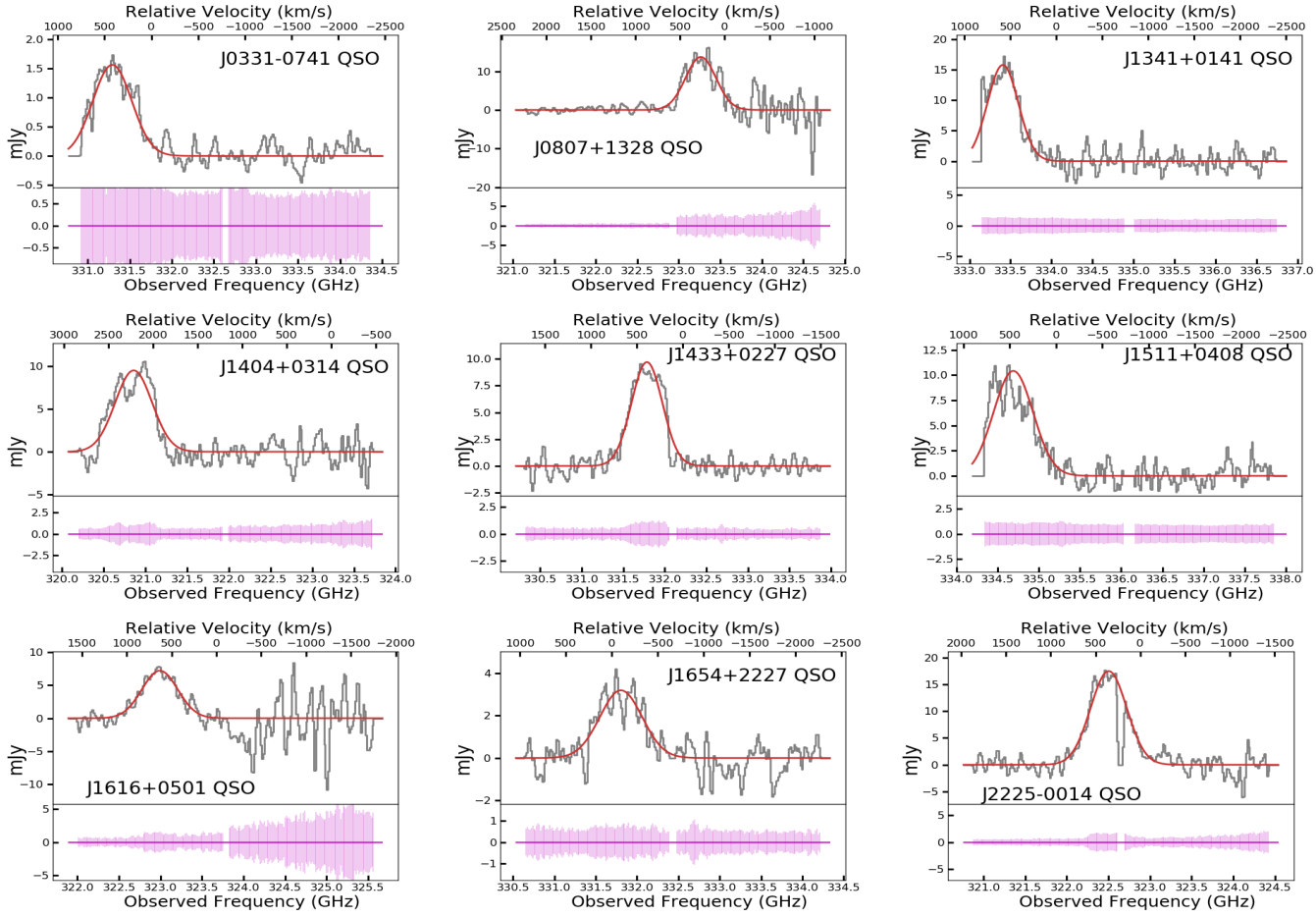

n

FIR-Faint Objs

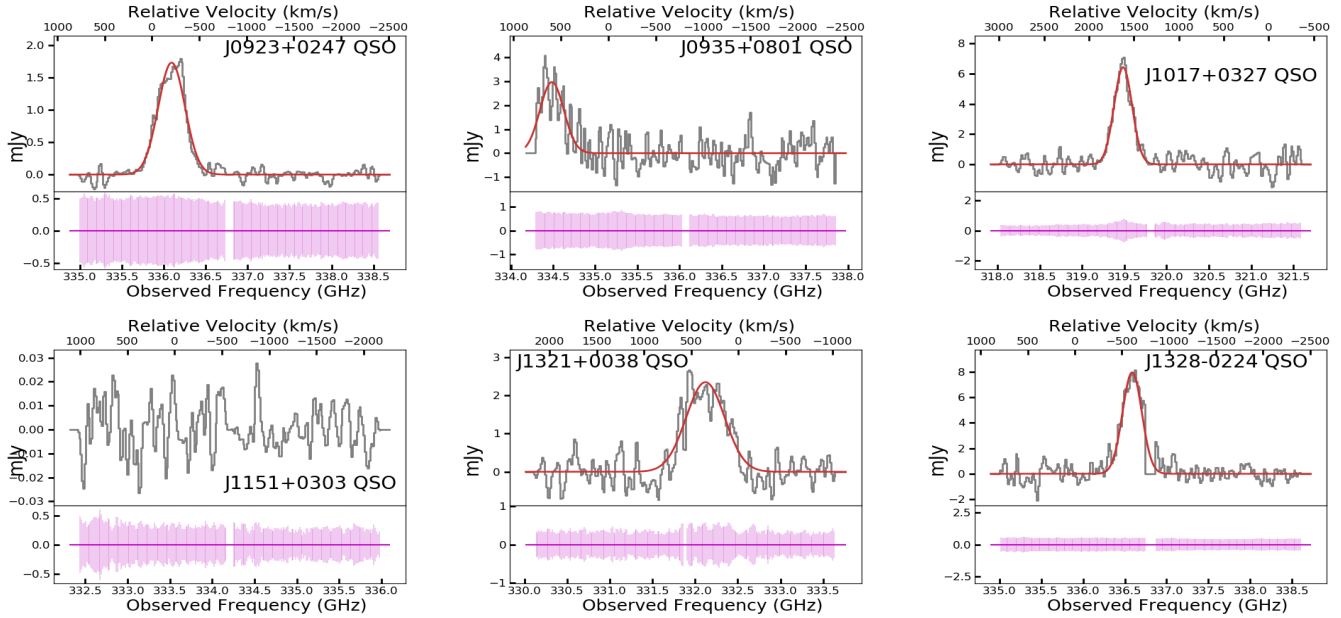

Figure 3.2
(Continued on the next page.)

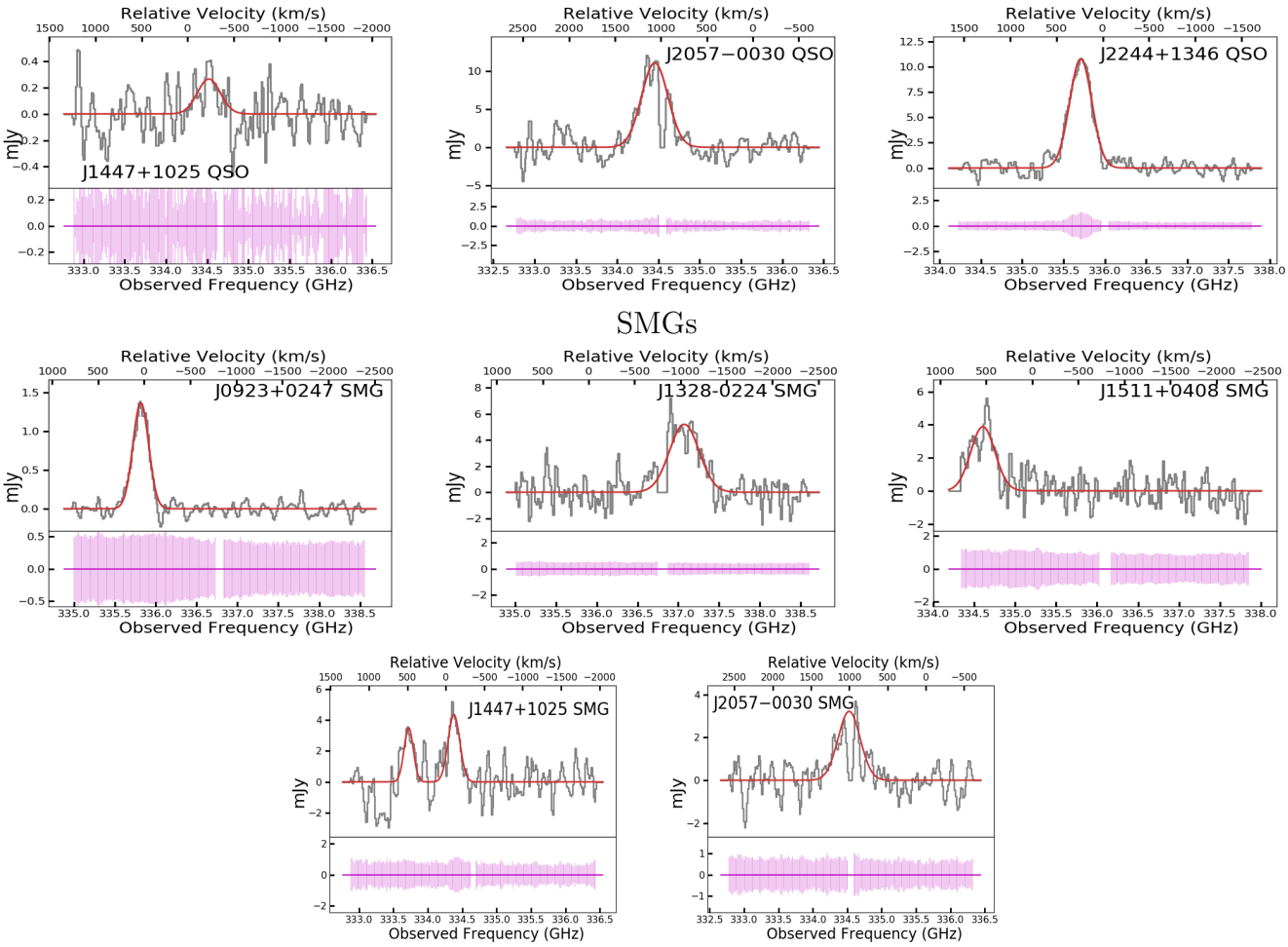

Figure 3.2: Spectra of the [C II] $\lambda 157.74\,\mu$m emission line for all the new ALMA observations reported in this work. FIR-bright sources are presented in the top three rows, FIR-faint sources are presented in the middle three rows, and accompanying SMGs are presented in the bottom two rows. For each spectrum the upper x-axis denote the velocity offsets with respect to the redshift derived from the Mg II broad emission lines (T11). Red lines show the Gaussian fits to the line profiles. RMS spectra are also included in the same scale as the flux spectrum except for J1151 where there is no [C II] detection and a high RMS.

FIR-Bright Objs.

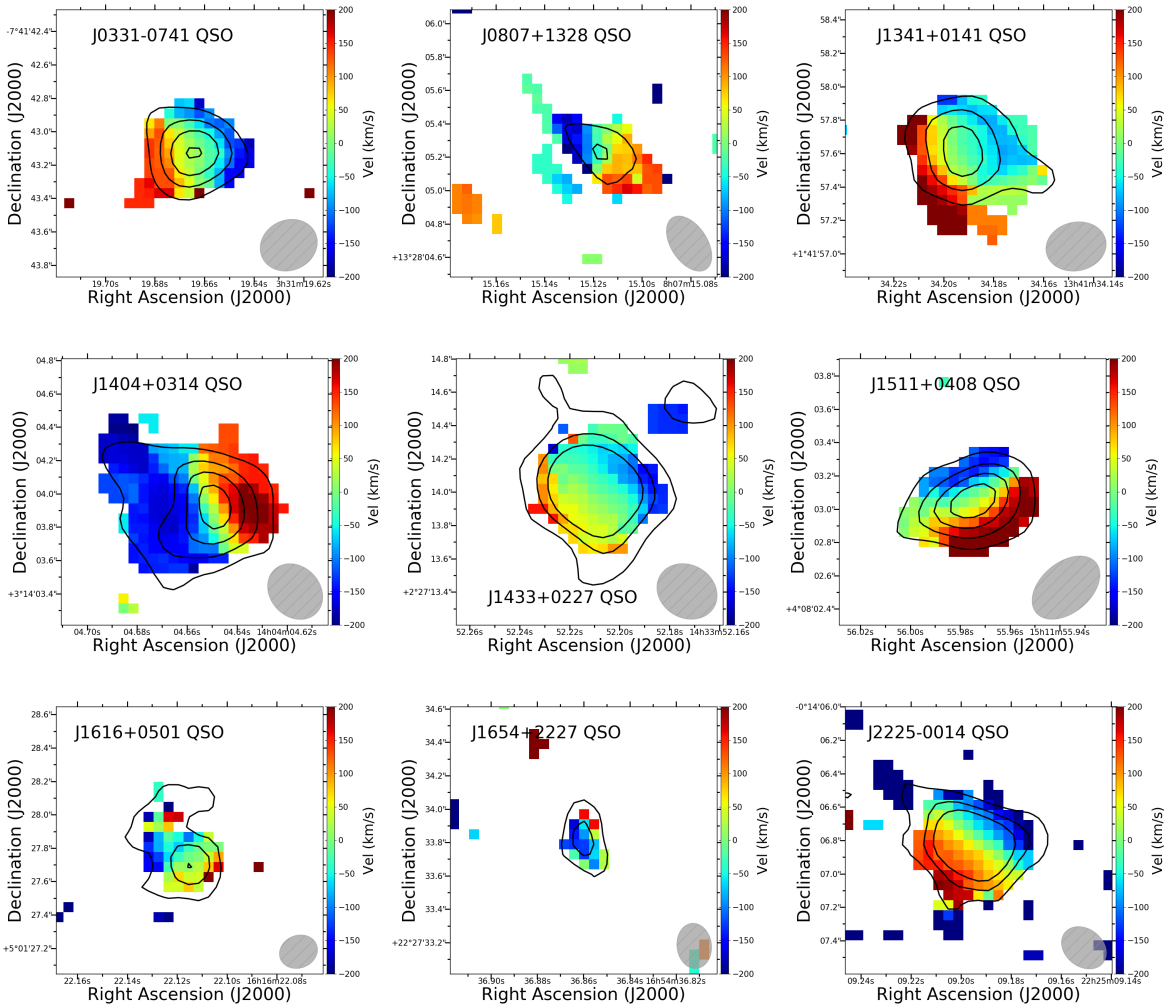

FIR-Faint Objs.

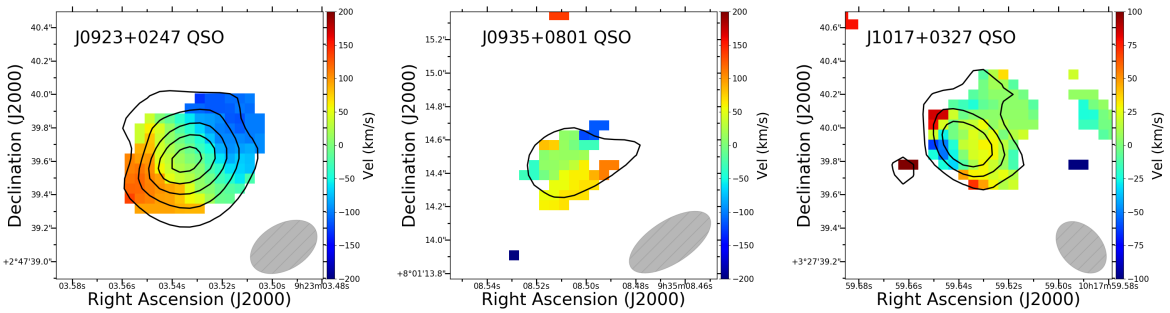

Figure 3.3
(Continued on the next page.)

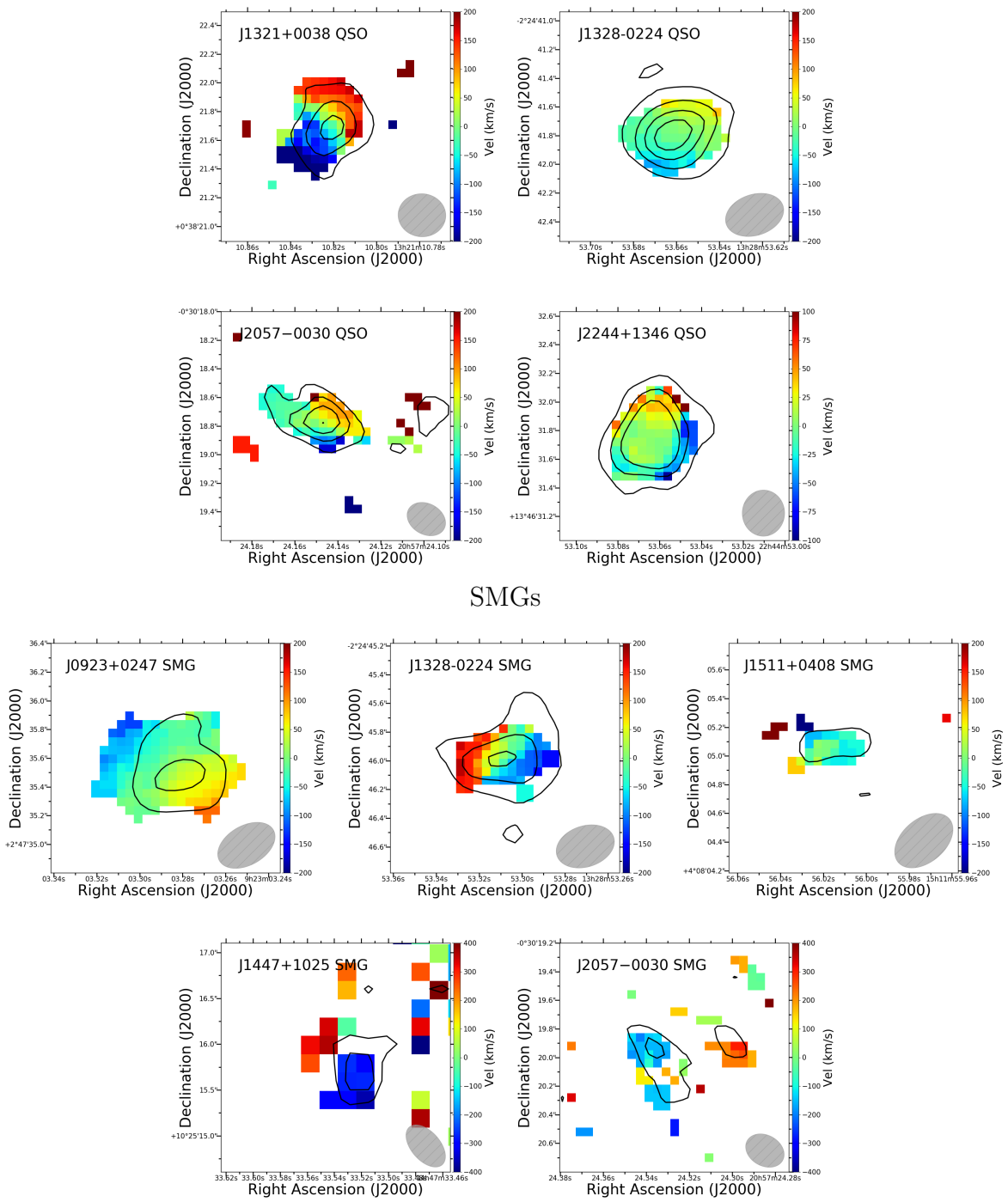

Figure 3.3: [C II] velocity maps for the FIR-bright sources in our sample (top three rows), FIR-faint sources (middle three rows), and the companion SMGs (bottom 2 rows), which are labeled in the figure. Black contours trace the [C II] emission line surface brightness at significance levels of 3, 6, 9, 12, and 15$-\sigma$. The ALMA beams are shown as hatched gray ellipses near the bottom-right of each panel.

FIR-Bright Objs.

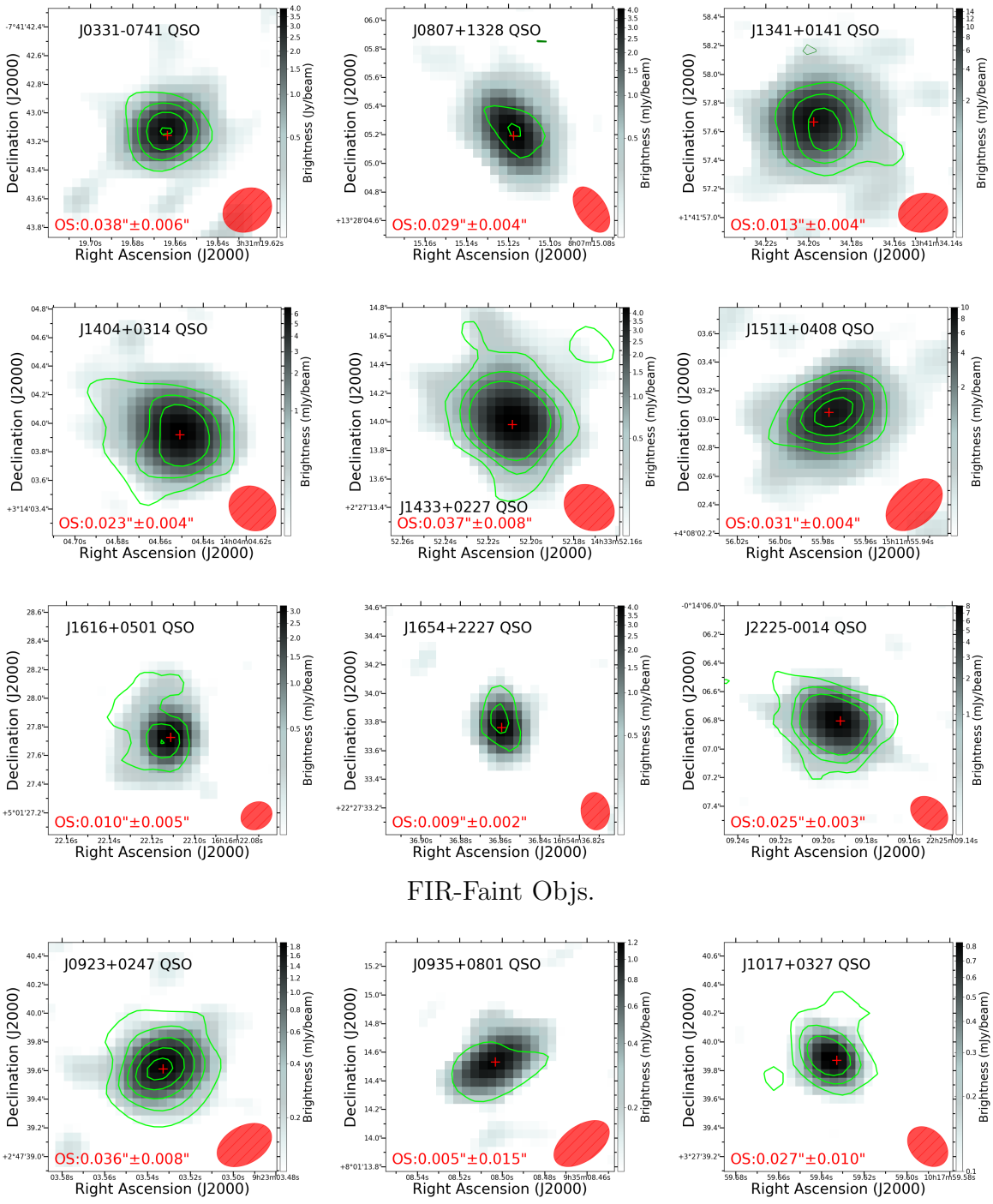

FIR-Faint Objs.

Figure 3.4
(Continued on the next page.)

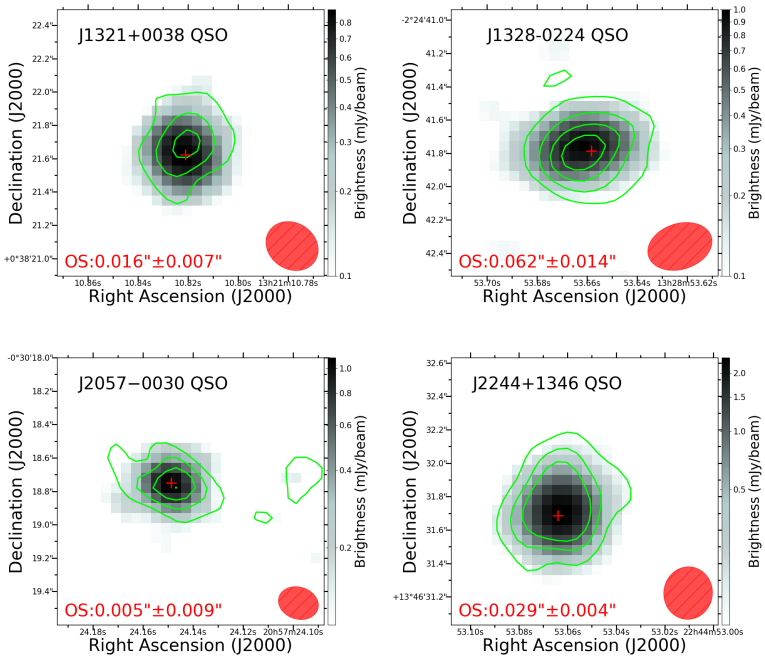

Figure 3.4: Small-scale continuum and [C II] line emission maps derived from the Cycle-6 ALMA data, for all the sources with clear detection of [C II] line emission. The FIR-bright sources in our sample are the top three rows, while the FIR-faint sources are the bottom three rows. For each source the gray-scale map traces the continuum emission, while the contours trace the [C II] line emission (i.e., surface brightness) at significance levels of 3, 6, and 9$-\sigma$. The line fluxes used for the contours were extracted from a spectral window spanning $\pm$500 km s^{-1} around the [C II] line peak of each source. The ALMA beams are shown as red ellipses near the bottom-right of each panel. The optical position from GAIA is marked with a red cross (+). In the bottom left of each image we list the Optical Separation (OS) along with the associated error.

3.2.1 Optical Center Separation

In Figure 3.4 we plot the continuum maps of our quasars, along [C II] emission contours. From The 2nd data release of the Gaia mission (Gaia Collaboration et al., 2018), crossed referenced with the PANN-Star 1 data base (Flewelling et al., 2016), we obtain the optical centers of our objects. We then compute Optical Separation (OS) as the separation between the Gaia optical center and the peak of continuum emission as determined by Gaussian fits. Each image in Figure 3.4 lists the OS along with the associated error. OS values have a range of 0.005" - 0.062" for our entire sample. Offsets of the optical center could be an indicator of dual-AGN or late stage major mergers (Orosz & Frey, 2013; Makarov et al., 2017). However these studies found OS values on scales of hundreds of milli-arcsecond scales, much larger than what we see. We also see that there is no correlation between host galaxy velocity gradients and OS. J1328-0224 is our object with the highest OS (62 mas) in our sample, but Figure 3.3 shows that it has a very low gradient of velocity with rather uniform values. In contrast, J2057-0030 has the lowest OS but we believe it to be a perturbed system with a tidal tale. Thus we do not consider the OS to be an indicator of mergers or perturbations for our sources.

3.3 SEDs and SFRs

We will rely on the rest frame ~ 152 μm FIR continuum emission to estimate the total FIR emission of our objects. This will allow us to determine the SFRs of the host galaxies and nearby SMGs using the well established relation between the FIR luminosity and the SFR (Kennicutt, 1989). For our FIR-faint objects this determination will be based only on the ALMA detection. For the FIR-bright objects, we will also use the 250, 350, and 500 μm *Herschel* measurements. We do not aim at performing a full modeling of the FIR Spectral Energy Distribution (SED), as the number of photometric points available do not allow for a determination of the several physical parameters necessary for that, but rather determine which set of SEDs better represent the observations.

The contribution to the FIR SED from the AGN should be small, commonly given as $\sim$ 10% (e.g., Schweitzer et al. 2006; Mor & Netzer 2012; Rosario et al. 2012; Lutz et al. 2016). In this work we assume that the FIR emission of the sources in our sample is dominated by dust heated as a result of SF activity (see full discussion and many references in Netzer et al. 2016 and Lani et al. 2017). The alternative view which involves AGN heated dust contributing significantly to the FIR SED has been discussed in several publications (e.g., Duras et al., 2017; Leipski et al., 2014; Siebenmorgen et al., 2015; Schneider et al., 2015) but will not be addressed in this work. However, we do account for an additional error of the 250 μm *Herschel*/SPIRE band due to contribution from AGN-heated dust (as explained in N14, we add in quadrature an uncertainty estimated as 0.32 times the AGN luminosity at 1450Å). Taking this effect into consideration increases the error of the 250 micron measurement on average by a factor of 1.67. ALMA absolute flux calibration in band-7 is claimed to be of the order of 10%. We add this uncertainty in quadrature to the errors quoted in Table 4.1.

Because we have very few measurements of the SEDs of our quasar (only the ALMA measurement for our FIR-faint objects) we use different methods to produce models of the FIR SEDs for our sources. The uncertainty of the ALMA measurement is roughly an order of

magnitude lower than those of the the *Herschel* points, thus the ALMA measurement usually dominates in all three methods we use.

For the first method we use the grid of FIR SEDs provided by Chary & Elbaz (2001, CE01). These 105 templates are unique in shape and scaling and are based on the star-forming (SF) galaxies at $0.8 < z < 2$. The best fit model is determined using the ALMA monochromatic luminosity and its associated uncertainty, while for the FIR-bright objects we also include the *Herschel* measurements (values and errors from N14, with the 250 μm flux error corrected as explained above). For FIR-faint objects the fit relies only on the ALMA measurement.

For the second method we scale the SED determined by Magnelli et al. (2012), which corresponds to an average from the most luminous SMGs in their work. As before, the *Herschel* measurements are included for those quasars with detections at 250, 350 and 500 μm. It should be stressed that this model is constructed from SMGs from a wide range of redshifts and which are less luminous than our own sample, with FIR luminosities of $\sim 10^{12} - 10^{13} L_{\odot}$. And, as SMGs, they have a *measured* dust emissivity of $\beta = 2.0 \pm 0.2$, much higher than our *assumed* general $\beta = 1.6$

For the third method we use a gray-body SED. Following the convention of similar works at high-redshift, we use a temperature of $T_{\rm d} = 47$ K and dust emissivity coefficient $\beta = 1.6$. However, we found that not all of our FIR-bright sources are well constrained by these parameters. Thus, we measure the best fit of a wider range of temperatures (40, 45, 50, 55, 60 and 70 K) and β values (1.5 and 1.7). It is possible that the FIR-faint objects are not truly well fit by $T_{\rm d} = 47$ K $\beta = 1.6$, but the determination of a best-fit temperature and β is only possible for the FIR-bright objects, due to their *Herschel* measurements. The mean χ^2 for our nine FIR-bright quasars is ~ 2 (for one degree of freedom). We show the SED fits in Figure 3.5 together with the best fit values, which are also reported in Table 4.1. We find that out of nine objects, seven are well fit by temperatures in the 40 to 50 K range. Two require higher temperatures: J0331–0741 is best fit by a $\beta = 1.7$ and $T_{\rm d} = 60$ K gray-body SED while J1616+0501 needs $\beta = 1.7$ and $T_{\rm d} = 70$ K. We briefly discuss these two cases next.

For J1616 all the *Herschel* photometric points are found more than 3σ above the CE01 best-fit template, which is dominated by the scaling to the ALMA measurement. The corresponding SFR from the gray-body best fit is 5275 $M_{\odot}\,{\rm yr}^{-1}$ even higher than the ~ 4200 $M_{\odot}\,{\rm yr}^{-1}$ found by N14 based on *Herschel* data only. A similar, although not as extreme case is J0331, for which N14 determined a SFR of ~ 2100 $M_{\odot}\,{\rm yr}^{-1}$, in good agreement with the value of 1922 $M_{\odot}\,{\rm yr}^{-1}$ we determine from the gray-body best fit. Clearly, the high SFRs determined for these sources are driven by their very high *Herschel* luminosities. The high gray-body temperatures, on the other hand, are the result of the correspondingly steep SEDs, which are found once the ALMA data are also taken into account.

Gray-body temperatures as high as $T_{\rm d} = 60-70$ are not expected for star-forming sources. However, temperatures as high as 70 or 80 K have been recently determined for a very small fraction of SMGs at high-redshift (Miettinen et al., 2017), so these rather high ISM temperatures might not be totally unusual in the most luminous sources, although more observations are necessary in order to confirm this.

Once the total IR luminosity is determined by integrating the SED over the 8-1000 μm range, the SFR is obtained using $\mathrm{SFR}/\mathrm{M}_\odot\,\mathrm{yr}^{-1} = \mathrm{L}_{\mathrm{FIR}}\ /10^{10}\mathrm{L}_\odot$, which assumes an Initial Mass Function (IMF) from Chabrier (2003). The results are presented in Table 4.1 as L_{CE} and $\mathrm{SFR}_{\mathrm{CE}}$ for the CE01 fits, L_{Mag} and $\mathrm{SFR}_{\mathrm{Mag}}$ for the Magnelli et al. (2012) fits, $L_{47\mathrm{K}\beta1.6}$ and $\mathrm{SFR}_{47\mathrm{K}\beta1.6}$ for the gray-body fit with fixed parameters $T_{\mathrm{d}} = 47$ K and $\beta = 1.6$, and as L_{bestGB} and $\mathrm{SFR}_{\mathrm{bestGB}}$ for the gray-body fit with T_{d} and β left as free parameters. For our total sample of 18 quasars, we see that the FIR-bright targets have a SFR range of $\sim 1000 - 3000\ M_\odot\,\mathrm{yr}^{-1}$, the FIR-faint objects have a range of $\sim 100 - 500\ M_\odot\,\mathrm{yr}^{-1}$, and the SFRs of the SMGs cover $\sim 60 - 600\ M_\odot\,\mathrm{yr}^{-1}$. The difference in the determined SFRs using the different methods illustrates the systematic uncertainties of these calculations.

Besides the FIR-bright sources presented in Figure 3.5, Table 4.1 also lists the SFRs obtained for the FIR-faint sources. The SED best-fit values for J1447 are based on the ALMA continuum upper limit previously determined. We found this object to have an extremely low SFR of $< 20\ M_\odot\,\mathrm{yr}^{-1}$, possibly indicating that effective starformation quenching has already occurred. The detection of [C II] in this host showcases how this line can be detected in the ISM of galaxies with very little on-going star formation.

In the following sections we will take the average SFR obtained from these methods as the representative SFR for each object. Errors will be computed as the maximum and minimum derived SFR.

3.4 The L_{AGN} versus L_{SF} plane

In the previous section, we covered how we created estimates of the SEDs of our sources. From these SEDs we can calculate the luminosity of Star Formation (SF) in the hosts. With the bolometric luminsoities derived in T11 from the flux of the 3000 Å emission, which is the underlying continuum of the Mg II λ2798 line measured in the same paper, we have an AGN related luminosity (L_{AGN}). Therefore we can now directly compare a measurement of the host (L_{SF}) with a measurement of the AGN (L_{AGN}), which is important to explore the growth of the entire system.

Figure 3.6 presents the L_{AGN} versus L_{SF} plane. FIR-bright and FIR-faint objects are shown with different colors, while the presence of companions are shown using different symbols. We determine a correlation coefficient of r = 0.55, p =0.02.

Since our luminosity ranges in L_{AGN} and L_{SF} are rather narrow, it is not possible to draw conclusions about how our sources compare with those trends found by previous works for L_{AGN} and L_{SF}-dominated sources. In fact, it has been a matter of great debate why the L_{AGN} versus L_{SF} plane shows significantly different trends depending on the way samples are defined (e.g., see discussion in Netzer et al. 2016). The answer to the apparent contradictory results seems to reside in the stochastic nature of AGN activity, with duty cycles much shorter than those that characterize star formation (e.g., Hickox et al., 2014; Volonteri et al., 2015; Stanley et al., 2015). In short, selecting samples based on SFR and binning them in AGN power, will give a representative L_{AGN}-L_{SF} relation since the rapid changes in AGN power ($\sim 10^{5-6}$ yr) will be smoothed out, while selecting them in L_{AGN} and binning in L_{SF} will mix-and-match objects selected from their 'unrepresentative' AGN luminosity and with very

different SF power. These observed differences, however, seem to saturate at the highest luminosities.

In Figure 3.6 we include a 1:1 $L_{\rm AGN}$-$L_{\rm SF}$ line as well as the trends determined by Netzer (2009) from observations at a wide redshift range and Rosario et al. (2012) at $z \lesssim 2$, both of which are defined for bright AGN but dominated by local samples in the case of Netzer (2009) and from samples drawn from deep field surveys in the case of Rosario et al. (2012), hence not including the most powerful AGN. It is therefore not surprising that our optically flux-limited selected sample of quasars on average, sits above both the Netzer (2009) and Rosario et al. (2012) relations. This is particularly true for the bright-FIR subsample.

In the bottom panel of Figure 3.6 we see that the individual distribution of $L_{\rm AGN}$ and $L_{\rm SF}$ do not clearly separate our FIR-bright and FIR-faint objects from each other. However, when we consider the $L_{\rm AGN}$ vs. $L_{\rm SF}$ plane in Figure 3.6 we see that the FIR-bright and FIR-faint objects occupy two distinct regions. This can also be seen in Figure 2 of Netzer et al. (2014) (as $\lambda L_{\lambda}(3000\text{Å})$) who analyzed the *Herschel* observations of $z \sim 4.8$ quasars, including all our FIR-bright and FIR-faint sources, and 20 further FIR-faint sources which have not been observed in ALMA. From this work it becomes clear that FIR-bright and FIR-faint sources dominate at the high and low-end of the BH mass distribution, respectively, but with no indication of a bimodality. We will return to the issue of the possible segregation observed in the $L_{\rm AGN}$ versus $L_{\rm SF}$ plane in Section 5.2.

Table 3.2: Compiled Offset List

Source	Target	[C II] − Mg II km s^{-1}	$L/L_{\rm Edd}$	log $L_{\rm IR}$	Mg II Paper
Trakhtenbrot et al. 2017	SDSS J033119.67–074143.1	+412	1.202	13.05	Trakhtenbrot et al. 2011
	SDSS J092303.53+024739.5	−213	0.6606	12.65	...
	SDSS J093508.49+080114.5	+588	0.741	12.37	...
	SDSS J132853.66-022441.6	−621	0.3548	12.40	...
	SDSS J134134.20+014157.7	+573	0.1819	13.51	...
	SDSS J151155.98+040803.0	+456	1.1819	13.31	...
Nguyen et al. 2020	SDSS J080715.11+132805.1	+256	0.447	13.08	...
	SDSS J101759.63+032739.9	+1605	0.549	12.34	...
	SDSS J132110.81+003821.7	+337	0.355	12.37	...
	SDSS J140404.63+031403.9	+2208	0.219	13.33	...
	SDSS J143352.21+022713.9	+379	1.230	13.15	...
	SDSS J144734.09+102513.1	−224	1.995	11.23	...
	SDSS J161622.10+050127.7	+620	0.537	13.38	...
	SDSS J165436.85+222733.7	−112	0.199	12.93	...
	SDSS J205724.14−003018.7	+1065	0.891	12.48	...
	SDSS J222509.19−001406.9	+340	0.617	13.35	...
	SDSS J224453.06+134631.6	+225	0.676	12.71	...
Decarli et al. 2018	SDSS J084229.43+121850.4	+310	0.7	12.20	De Rosa et al. 2011
	SDSS J130608.26+035626.3	+757	0.792	12.50	Kurk et al. 2007
	CFHQS J1509-1749	+63	0.68	12.59	Willott et al. 2010
	CFHQS J2100-1715	−245	0.49	11.77	...
	PSO J231.6576–20.8335	−340	0.48	13.04	Mazzucchelli et al. 2017
	VIKING J1048-0109	+583	...	12.92	Venemans in Prep.
	VIKING J2211-3206	+139	...	12.24	...
	VIKING J2318-3113	−20	...	12.92	...
Willott et al. 2013	CFHQS J0210−0456	−230	2.4	11.41	Willott et al. 2010
Willott et al. 2015	CFHQS J0055+0146	+988	0.62	11.69	...
	CFHQS J2229+1457	−13	2.4	11.09	...
Willott et al. 2017	CFHQS J2329−0301	−24	1.3	10.95	...
	PSO J167.6415−13.4960	+308	1.2	12.43	Venemans et al. 2015
Venemans et al. 2012	ULAS J112001.48+064124.3	−474	1.2	12.30	De Rosa et al. 2014
Venemans et al. 2016	VIKING J234833.34−305410.0	+486	0.18	12.73	...
	VIKING J010953.13−304726.3	+1690	0.24	12.19	...
	VIKING J030516.92−315056.0	+374	0.68	12.93	...
Venemans et al. 2017	ULAS J134208.10+092838.6	+503	1.5	11.98	Banados et al. 2018
Mazzucchelli et al. 2017	PSO J338.2298+29.5089	+818	0.11	12.45	Mazzucchelli et al. 2017
	PSO J323.1382+12.2986	+230	0.44	12.11	...
Banados et al. 2015	PSO J036.5078+03.0498	+566	0.96	12.88	Venemans et al. 2015
Wang et al. 2016	SDSS J010013.02+280225.8	+1019	0.95	12.54	Wu et al. 2015

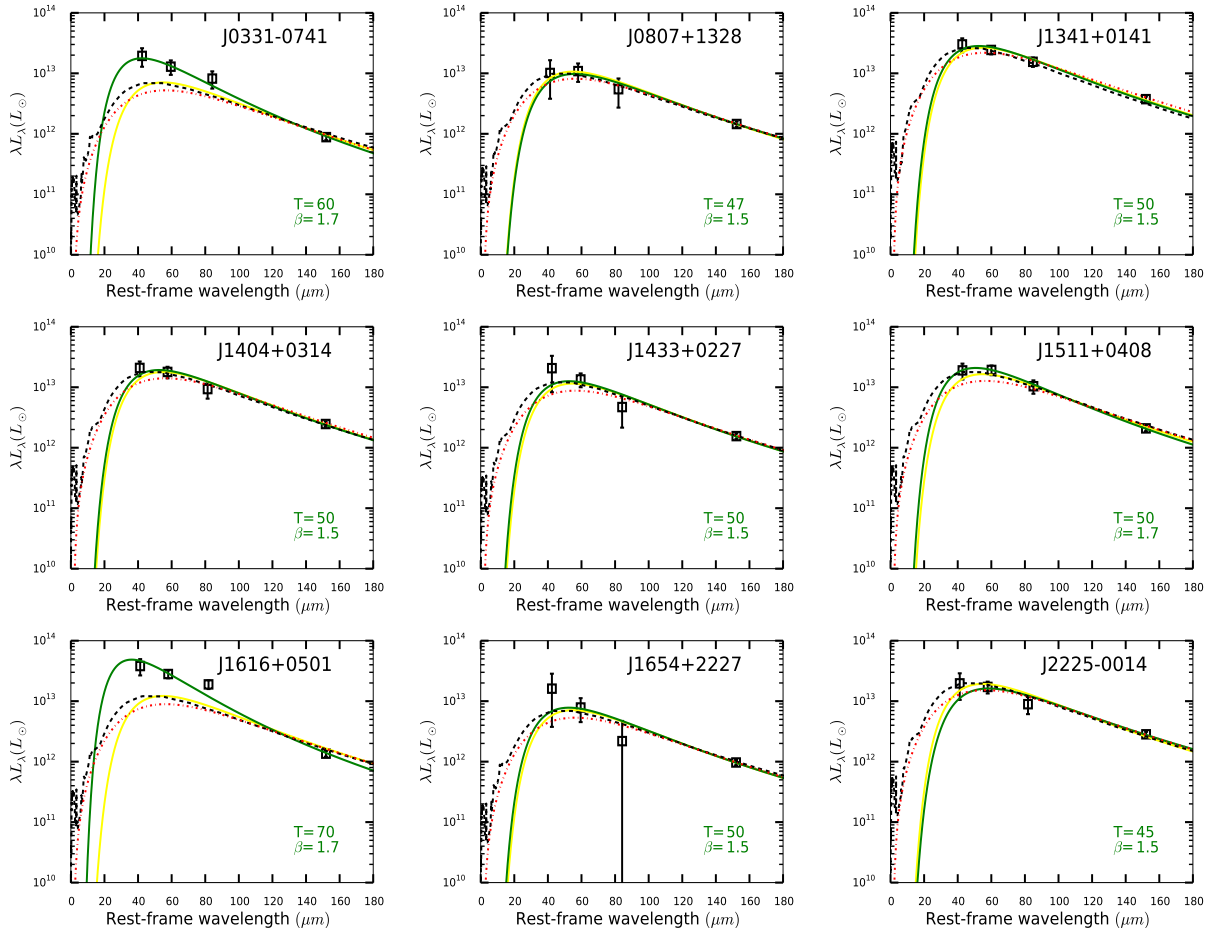

Figure 3.5: FIR SEDs for the nine FIR-bright quasars in our sample. Data points correspond to *Herschel*/SPIRE measurements at 250, 350 and 500 μm and ALMA detections at 895 μm (in the observed frame). For each source four model SEDs are presented: black-dashed lines represent the best-fitting FIR template from Chary & Elbaz (2001) while red-dotted lines represent the scaled SED from Magnelli et al. (2012). A scaled gray-body SED with $T_{\rm d} = 47\,{\rm K}$ and $\beta = 1.6$ is shown with a solid-yellow line, while a best fit model gray-body SED is shown with solid-green lines. The gray-body best fit parameters are included for each source. Best fit T and β are listed in green in the bottom right corner.

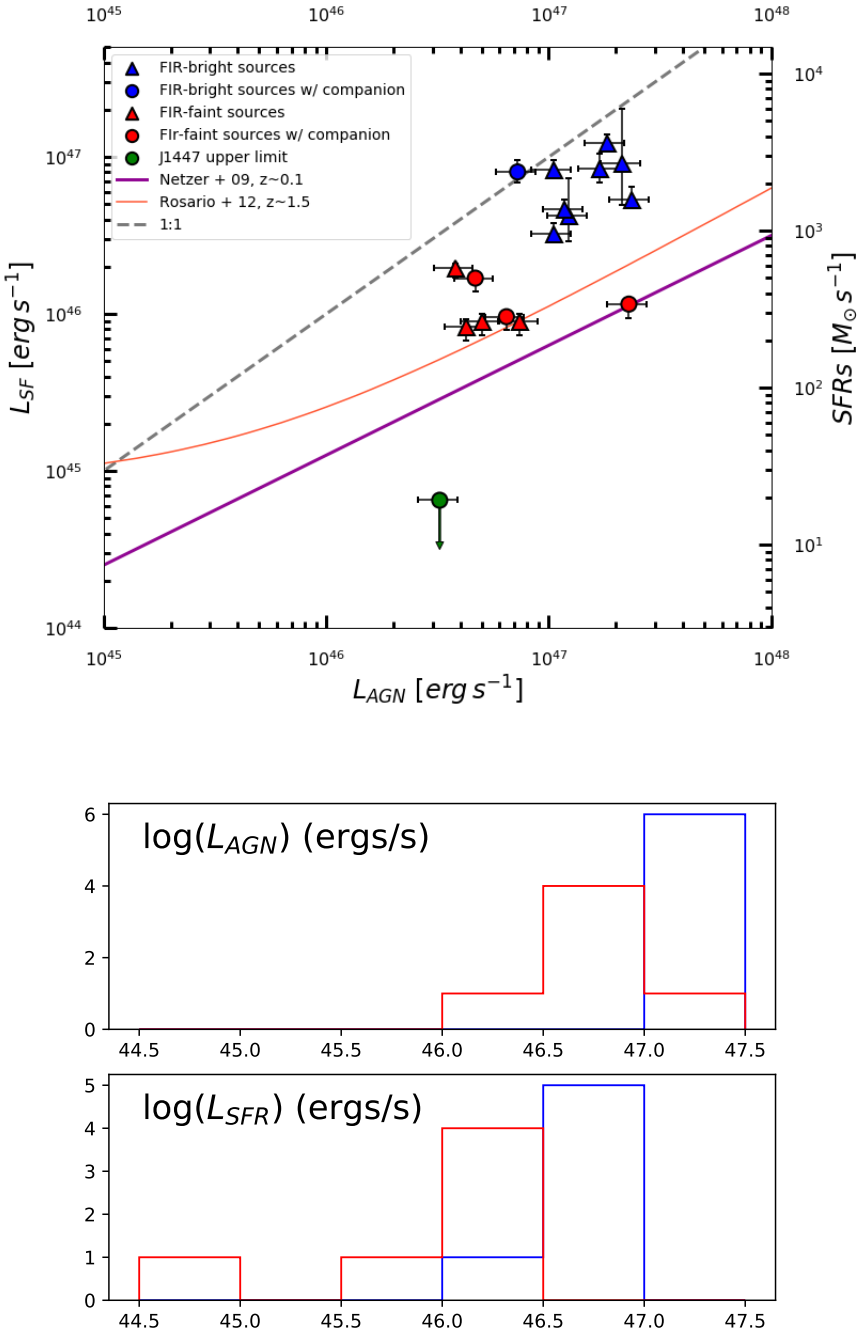

Figure 3.6: **Top:** $L_{\rm SF}$ versus $L_{\rm AGN}$ for our FIR-bright (blue markers) and FIR-faint sources (red markers), as well as the upper limit of J1447 (green marker) with an arrow to indicate it is an upper limit. Those sources with companions are marked as a circle. The orange curve for redshift $0.8 - 1.5$ from Rosario et al. (2012) and scaled up by a factor of two to allow for the difference between L(60 μm) used in that paper and the $L_{\rm SF}$ used in our work. The correlation for AGN dominated sources is shown as a solid purple and is taken from Netzer (2009) as $\rm L_{SF} \simeq 10^{43}(L_{AGN}/(10^{43} erg\,s^{-1}))^{0.7}$. The dashed straight line corresponds to $L_{\rm AGN}$ = $L_{\rm SF}$, shown for reference. **Bottom:** Logarithmic distributions of $L_{\rm SF}$ and $L_{\rm AGN}$ in units of ergs s^{-1}.

Chapter 4

Dynamical and Dust Masses

4.1 Dynamical Masses

The [C II] line can be used to estimate the dynamical masses ($M_{\rm dyn}$) of the quasar host galaxies and the companion SMGs. We use the same method as several other studies of [C II] and CO emission in high-redshift sources (e.g., Venemans et al. 2016), which assumes the [C II]-traced ISM is arranged in an inclined, rotating disk (Wang et al., 2013; Willott et al., 2015; Venemans et al., 2016), and determine $M_{\rm dyn}$ as:

$$M_{\rm dyn} = 9.8 \times 10^8 \left(\frac{D_{\rm [C\,II]}}{\rm kpc}\right) \left[\frac{\rm FWHM\,[C\,II]}{100\ \rm km\,s^{-1}}\right]^2 \frac{1}{\sin^2({\rm i})}\ M_\odot\ . \tag{4.1}$$

In this relation $D_{\rm [C\,II]}$ is the size of the [C II]-emitting region measured by the deconvolved major axis of the Gaussian fit of said region (see Table 4.1). The $\sin({\rm i})$ term reflects the inclination angle between the line of sight and the polar axis of the host gas disks, with the circular velocity given as $v_{\rm circ} = 0.75 \times {\rm FWHM}/\sin({\rm i})$. i is determined from the ratio $\cos({\rm i}) = (a_{\rm min}/a_{\rm maj})$, where $a_{\rm min}$ and $a_{\rm maj}$ are the semi-minor and semi-major axes of the [C II] emitting regions, respectively. These masses can be found in Table 4.1, where we list $M_{\rm dyn}$ as well as its inclination uncorrected value (i.e., $M_{\rm dyn}^{uncorr} = M_{\rm dyn} \times \sin^2({\rm i})$).

We find that the FIR-bright and FIR-faint systems have comparable M_{dyn} values, with a mean of $8\times10^{10}\ M_\odot$. We also note that among the interacting SMGs reported in this work the companion to J1447 is of particular interest. Individually its two [C II] spectral components, each with unresolevd sizes, would correspond to systems with comparable dynamical masses found at the lower end of the observed range presented in Table 4.1. Therefore they would represent a major merger between these two components, while a likely minor merger with the quasar host. Note, however, that the dynamical mass of the J1447 host is also particularly uncertain, due to the weakness of the [C II] detection.

This method of deriving the dynamical mass carries significant uncertainties, due to several assumptions required to derive them, and to the limited spatial resolution data available for our systems. A large contributor to the error is our measurement of the major and minor

axis of the [C II] emitting region, from which we derive i and $D_{[\mathrm{C\,II}]}$. We estimate a mean error of 0.44 dex by propagating systematic uncertainties and the uncertainties of our measured values.

However, the most significant assumption is that we are observing inclined rotating disks. 7/9 of our FIR-bright and possibly only 3/7 of our FIR-faint objects show clear indications of a smooth and coherent velocity gradient, as can be seen in Figure 3.3. Furthermore, note that a even a smooth and coherent velocity gradient does not guarantee a rotation dominated host galaxy. We can compute the dynamical masses assuming the case of pure dispersion-dominated gas (Decarli et al., 2018):

$$M_{\mathrm{Disp}} = \frac{3}{2}\frac{a_{\mathrm{maj}}\,\sigma_{line}^2}{G} \tag{4.2}$$

where σ_{line} is the line width of the Gaussian fit of the [C II] spectrum, G is the gravitational constant, and a_{maj} again is the major axis of the [C II]-region. We find that the dynamical masses we derive from assuming dispersion-dominated gas is lower than both the inclination corrected and non-corrected dynamical masses derived from assuming a rotating disk, with a mean of 2.4 $\times 10^{10}$ $M_\odot$ for M_{Disp} (see Table 4.1 Galaxy Properties II). Dynamical masses derived from assuming dispersion-dominated gas can be regarded as a lower limit to the true dynamical mass. We will use the dynamical masses obtained assuming an inclined, rotating disk throughout this rest of the work in order to be comparable to similar studies in the literature.

4.2 Dust masses

The underlying continuum emission at observed wavelength $\sim$ 152 μm can also be used to calculate dust masses for our objects assuming that the FIR continuum flux originates from optically thin dust at these wavelengths. Using the same methods as in Dunne et al. (2000) and Beelen et al. (2006) (see also, Scoville et al. 2016), the dust mass can be calculated as:

$$M_{\mathrm{d}} = \frac{S_{\lambda rest} D_L^2}{\kappa_{\mathrm{d}}(\lambda_{rest}) B(\lambda_{rest}, T_{\mathrm{d}})} \tag{4.3}$$

where $\kappa_{\mathrm{d}}(\lambda) \propto \lambda^{-\beta}$ is the wavelength dependent dust mass opacity, $S_{\lambda rest}$ is the continuum flux density at λ_{rest}, $B(\lambda_{rest}, T_{\mathrm{d}})$ is the monochromatic value of the Planck function at λ_{rest} for temperature T_{d}, and D_L is the luminosity distance. κ_{d} is found to be 0.077 m^2 kg^{-1} at 850 μm (Dunne et al., 2000), and hence, $\kappa_{\mathrm{d}}(\lambda_{rest}) = 0.077\ (850/\lambda_{rest})^{\beta}$ m^2 kg^{-1}. To calculate the dust mass we assume $T_{\mathrm{d}} = 47$ K and $\beta = 1.6$.

We note from Equation 4.3 that the only formal error comes from the measurement of the continuum flux, while systematic errors will arise from our assumption of the adopted SED and the opacity coefficient, which will dominate. However, as we are using very similar parameters to those adopted in the literature a direct comparison of results is possible.

We derive dust masses for our full sample of 16 continuum detected quasars and find a range of $M_{\mathrm{d}ust} \sim 2 - 15 \times 10^8 M_\odot$ (see Table 4.1). Upper limits of $\sim 10^8 M_\odot$ and $\sim 10^7 M_\odot$

are found for J1151 and J1447 hosts, respectively. The average value is larger for FIR-bright objects than for FIR-faint objects, with dust masses of $10^{9.0}$ and $10^{8.4} M_{\odot}$, respectively. In Table 4.1 we also determine dust masses for the FIR-bright objects using the best fit values of T_{bestGB} and β_{bestGB} discussed in Section 3.3. However, we note that due to the small range of T and β and the dominance of the continuum flux density and luminosity distance, the differences in these calculations from assuming $T_{\rm d} = 47$ K and $\beta = 1.6$ are minor.

4.3 Gas Masses

We can determine gas masses, M_{gas}, making use of a gas-to-dust ratio (GDR) of 100, as determined at low-z (Draine et al., 2007). Recent studies comparing gas mass estimates obtained from CO line measurements and dust masses obtained from FIR emission have given a wide range of GDRs for high-redshift systems ($\sim 30 - 100$) (Ivison et al., 2010; Aravena et al., 2016c; Banerji et al., 2017). This is an unexpected result, since it is well established that high-z galaxies are characterized by lower metallicities at all galaxy masses (Lian et al., 2018) and that the GDR is inversely proportional with metallicity (Rémy-Ruyer et al., 2014; De Vis et al., 2019). However, as discussed in Aravena et al. (2016c) and Banerji et al. (2017), another interpretation for these results is to assume a 'normal' GDR and revisit the determination of the CO luminosity to total gas conversion factor. Both, the GDR and CO luminosity to total gas fraction are highly dependent on galaxy properties, such as surface density, compactness, and particularly, metallicity. In summary, and for a more straight forward comparison with other works, we adopt a GDR of 100.

Gas masses are presented in Table 4.1 and are found to be large, in the $10^{10-11} M_{\odot}$ range. For four of our FIR-bright systems M_{gas} are larger than the dynamical masses (assuming a rotating disk) by factors of up to three, while for only one FIR-faint system $M_{gas} \sim 0.9 \times M_{\rm dyn}$, the remaining showing factors ranging from 0.2 to 0.7.

In general the estimated ISM masses for our quasars are comparable to their dynamical masses. For our FIR-bright sources, 6/9 show $M_{gas} \geq M_{\rm dyn}$, by factors 1-3 (the unphysical finding that $M_{gas} > M_{\rm dyn}$ would be alleviated had we adopted a GDR as low as 30, as discussed above). This is not seen for the FIR-faint sources, suggesting that FIR-bright objects are more gas rich than FIR-faint systems. Defining $f_{gas} \equiv M_{gas}/M_{\rm dyn}$, we find for those objects where $M_{gas} < M_{\rm dyn}$ that $f_{gas} = 0.2 - 1.0$.

4.4 The Main Sequence at $z \sim 5$

We want to compare our full quasar sample with galaxies found on the stellar mass – SFR sequence for starforming systems, the 'main sequence' (MS), at similar redshifts. However, we only have estimates for the total dynamical and gas masses of our quasar hosts, not of their stellar masses. In principle, these could be obtained calculating $M_{\star} = M_{\rm dyn} - M_{gas}$. From the measured values there is a strong indication that most of the quasars hosts are very gas rich, with $M_{gas} = 0.3 - 4.0\ M_{\star}$, for those objects where $M_{gas} < M_{\rm dyn}$, and possibly higher for those objects where $M_{gas} > M_{\rm dyn}$. As already explained, the uncertainties on these values are significant.

An alternative approach is to adopt a gas fraction measured in non-active high-z galaxies where the stellar mass can be determined directly, which is not possible for our sample because of the dominance of the AGN continuum at rest-frame near-IR and optical bands. These determinations have been done out to $z \sim 4$ (Schinnerer et al., 2016; Dessauges-Zavadsky et al., 2017; Darvish et al., 2018; Gowardhan et al., 2019), and found $f_{gas} \sim 0.5 - 0.8$ (considering no dark matter), where a strong dependence with redshift and no correlation with environment are also seen (Darvish et al., 2018). We can then conservatively assume that for our systems $f_{gas} = M_{gas}/M_{dyn} = 0.6$ and therefore $M_\star = 0.4\ M_{\rm dyn}$.

In Figure 4.1, we plot two MS curves. One is the parameterization given in Equation (9) of Schreiber et al. (2015) for redshift ranges $4 < z < 5$, after correcting for the different adopted IMF (Schreiber et al. 2015 uses a conversion factor of SFR to L_{SF} 1.7 times larger than our own). The second curve is from Tomczak et al. (2016), for galaxies at redshifts $0.5 < z < 4$. Both MS curves agree well with each other.

We find that the majority of our sources lie above the MS curves. If we used dynamical mass values derived from assuming dispersion-dominated gas, our objects would shift to the lower stellar mass regime and sit even higher above the MS, as seen in Figure 4.1. Clearly, all of our FIR-bright quasars are found in the starbursting domain and at least 1 dex from the MS. Their SFRs are only comparable to the brightest known SMGs. Some of the FIR-faint sources sit within 1σ of the MS of starforming galaxies at those early epochs, but again, the majority of our faint sources sit above the MS. Note that our division into FIR-bright and FIR-faint sources is completely arbitrary (as described in Section 2.1), and the determined SFRs for our full sample is indeed a continuous distribution, as shown in the bottom panel of Figure 3.6.

Table 4.1: Galaxy Properties I

Subsample	Target		$\log L_{\rm CE}$	$\log L_{\rm Mag}$	$\log L_{\rm 47K\beta 1.6}$	$\log L_{\rm bestGB}$	$T_{\rm bestGB}$	$\beta_{\rm bestGB}$	$\rm SFR_{CE}$	$\rm SFR_{Mag}$	$\rm SFR_{47K\beta 1.6}$	$\rm SFR_{bestGB}$
	ID	Object	($L_\odot$)	($L_\odot$)	($L_\odot$)	($L_\odot$)	(K)		($M_\odot\,\rm yr^{-1}$)	($M_\odot\,\rm yr^{-1}$)	($M_\odot\,\rm yr^{-1}$)	($M_\odot\,\rm yr^{-1}$)
Bright	J0331	QSO	12.99	12.88	12.89	13.3	60	1.70	985	756	776	1922
	J0807	QSO	13.15	13.07	13.07	13.0	47	1.50	1405	1175	1170	1082
	J1341	QSO	13.56	13.50	13.46	13.5	50	1.50	3613	3164	2911	3137
	J1404	QSO	13.40	13.31	13.29	13.3	50	1.50	2496	2033	1959	2135
	J1433	QSO	13.23	13.10	13.10	13.1	50	1.50	1688	1268	1262	1394
	J1511	QSO	13.40	13.26	13.26	13.4	50	1.70	2496	1838	1805	2262
	J1511	SMG	12.25	12.40	12.41	—	—	—	176	250	256	—
	J1616	QSO	13.23	13.11	13.13	13.7	70	1.70	1688	1289	1336	5275
	J1654	QSO	12.99	12.89	12.89	12.9	50	1.50	985	770	778	865
	J2225	QSO	13.44	13.34	13.32	13.3	45	1.50	2766	2201	2113	1796
Faint	J0923	QSO	12.56	12.68	12.69	—	—	—	362	477	487	—
	J0923	SMG	12.16	12.27	12.28	—	—	—	144	187	191	—
	J0935	QSO	12.28	12.41	12.42	—	—	—	192	255	261	—
	J1017	QSO	12.25	12.37	12.38	—	—	—	176	237	242	—
	J1151	QSO	11.93	12.12	12.13	—	—	—	86	131	134	—
	J1321	QSO	12.28	12.41	12.42	—	—	—	192	254	260	—
	J1328	QSO	12.32	12.43	12.44	—	—	—	207	270	276	—
	J1328	SMG	11.86	12.04	12.05	—	—	—	72	109	112	—
	J1447†	QSO	<11.06	<11.28	<11.29	—	—	—	<12	<19	<19	—
	J1447	SMG	12.68	12.79	12.80	—	—	—	482	620	634	—
	J2057	QSO	12.39	12.51	12.52	—	—	—	246	326	333	—
	J2057	SMG	11.83	11.99	12.00	—	—	—	67	98	100	—
	J2244	QSO	12.65	12.73	12.74	—	—	—	444	536	548	—

Table 4.1 continued.

Table 4.1: Galaxy Properties II

Subsample	Target		$\log M_{\rm dyn}^{uncorr}$	$\log M_{\rm dyn}$ [a]	$\log M_{\rm Disp}$	$\log M_{dust}$ [b]	$\log M_{BF}$ [c]	$\log M_{\rm BH}$ [d]	$M_{\rm dyn}/M_{\rm BH}$	$\dot{M}_*/\dot{M}_{\rm BH}$ [e]
	ID	Object	($M_\odot$)	($M_\odot$)	($M_\odot$)	($M_\odot$)	($M_\odot$)	($M_\odot$)		
Bright	J0331	QSO	10.6	10.8	10.4	8.8	8.6	8.8	88	572
	J0807	QSO	10.7	10.8	10.5	9.0	9.0	9.2	33	65
	J1341	QSO	10.7	10.9	10.5	9.4	9.4	9.8	11	111
	J1404	QSO	10.9	11.4	10.7	9.2	9.2	9.5	81	130
	J1433	QSO	10.6	11.0	10.4	9.0	9.0	9.1	131	38
	J1511	QSO	10.8	10.9	10.6	9.1	9.0	8.4	264	183
	J1511	SMG	10.8	10.8	10.6	...	...	...	...	...
	J1616	QSO	10.9	11.1	10.7	8.9	8.7	9.4	49	71
	J1654	QSO	10.8	10.8	10.6	8.8	8.8	9.6	18	51
	J2225	QSO	10.7	11.0	10.5	9.2	9.2	9.3	53	82
Faint	J0923	QSO	10.5	10.9	10.4	8.6	...	8.7	158	60
	J0923	SMG	10.2	10.3	10.1	...	...	...	...	...
	J0935	QSO	10.4	10.6	10.3	8.3	...	8.8	56	20
	J1017	QSO	10.0	11.0	9.8	8.3	...	8.7	178	32
	J1151	QSO	...	...	...	<8.0	...	8.8	...	27
	J1321	QSO	10.8	11.0	10.6	8.3	...	9.0	110	30
	J1328	QSO	10.1	10.8	9.8	8.3	...	9.1	50	24
	J1328	SMG	10.8	11.0	10.7	...	...	...	...	...
	J1447†	QSO	10.2	11.1	10.0	<7.2	...	8.0	1214	3
	J1447	SMG	10.0	10.2	9.8	8.7	...	...	..	...
	J2057	QSO	10.5	10.6	10.3	8.4	...	9.2	21	8
	J2057	SMG	11.0	11.0	10.8	7.9	...	...	..	...
	J2244	QSO	10.3	10.7	10.1	8.6	...	8.8	126	84

†Dynamical masses based on estimate of the size of the J1447 host.

[a]Calculated using the inclination-angle corrections derived from the sizes of the [C II]-emitting regions.

[b]Calculated assuming the CE01-based SFRs.

[c]Best fit values are T_{bestGB} and β_{bestGB} from Table Galaxy Properties I

[d]Black hole masses taken from T11.

[e]Calculated assuming $\dot{M}_{\rm BH} = (1-\eta)\, L_{\rm bol}/\eta\, c^2$, with $\eta = 0.1$.

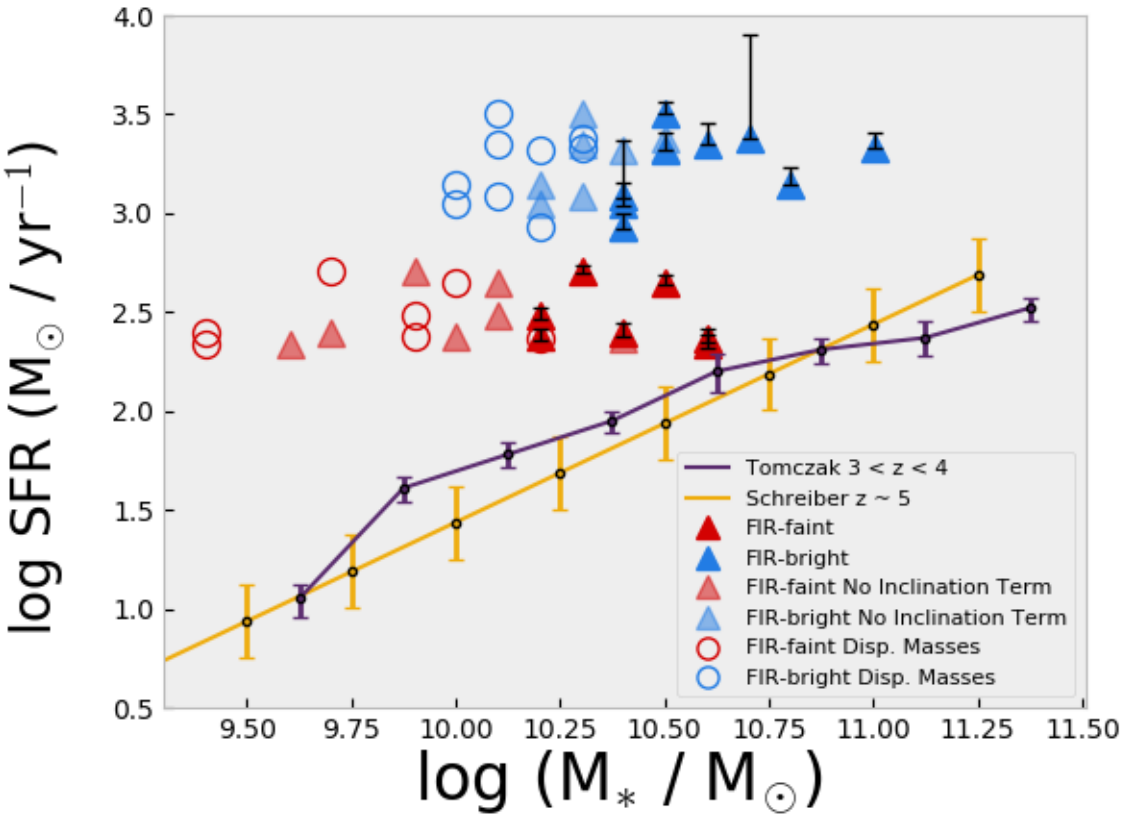

Figure 4.1: Stellar mass versus Star Formation Rate – the main sequence of starforming galaxies – for our quasars. Bright and faint FIR sources are shown with different colors. Only eight FIR-faint objects are plotted as one FIR-faint source does not have a $M_{\rm dyn}$ determined. The dynamical mass and SFR values are taken from Table 4.1. We assume $M_\star = 0.4 M_{\rm dyn}$, as explained in Section 4.4. We include the MS curves given in Equation (9) of Schreiber et al. (2015) (shown in yellow) and that of Tomczak et al. (2016) (in purple). The opaque red and blue triangles are our inclination corrected dynamical masses, while the transparent triangles are the inclination *uncorrected* dynamical masses. The dynamical masses calculated assuming dispersion dominated gas are plotted as circles.

Chapter 5

Growth of SMBHs and Galaxies Through Mergers

5.1 SMBH–Host Galaxy Mass Relation

In Figure 5.1, we plot the stellar masses of our quasar hosts against their black hole masses for the full sample of nine FIR-bright and eight FIR-faint quasars detected in [C II]. As before, we have adopted $M_\star = 0.4 M_{\rm dyn}$. However, it is likely that the real values of $M_\star$ would broaden the observed distribution, which now corresponds to a net shift of the observed $M_{\rm dyn}$ distribution. Black Hole masses were taken from T11 and are based on Mg II measurements. We find that the average black hole mass of our sample is $10^{9.2} M_\odot$, with a slight difference between the black hole properties of FIR-bright and -faint objects. FIR-bright objects having an average $M_{\rm BH}$ of $10^{9.4} M_\odot$ and Eddington ratio of $L/L_{\rm Edd} \sim 0.65$, while FIR-faint objects have an average $M_{\rm BH}$ and Eddington ratio of $10^{8.9} M_\odot$ and 0.78 respectively. We find a mean $M_{BH}/M_\star$ ratio of 1/19, with FIR-bright sources having $M_{BH}/M_\star = 1/15$ and FIR-faint systems 1/28.

We compare our sample with the local massive elliptical galaxies (Kormendy & Ho, 2013), Figure 5.1 shows the positions of local galaxies with a $M_{BH}/M_\star$ ratio ranging from $\sim 1/100$ to $\sim 1/1000$, the ratios being strongly correlated with mass. While the black hole masses of our sample of high-z luminous quasars are found at similar values as seen in the local universe, the stellar masses are on average one order of magnitude lower. This is similar to the results found by other groups and is in good agreement with the direct detection of two quasars hosts at $z \sim 4$ (Targett et al., 2012). In particular, Netzer et al. (2014) determined M_{BH} for 9 *Herschel* detected sources (the same sources presented in this work) and 29 undetected quasars (9 included here) at $z \sim 4.8$, hence improving the statistics of the FIR-faint sources. They found median BH mass for the FIR-bright sources of $10^{9.3}$ $M_\odot$, and a median for the FIR-faint sources of $10^{8.9}$ $M_\odot$, which is consistent with our own result of $10^{8.8}$ $M_\odot$. Many high-redshift samples lack robust $M_{\rm BH}$ measurements however Venemans et al. (2016) is a thorough, but small, high-redshift sample with $M_{\rm BH}$ values taken from De Rosa et al. (2014). When compared to our own sample we see that they sit between the FIR-bright and FIR-faint objects with an average $M_{BH}/M_\star$ ratio of 1/19, the same as our sample. In terms of

their AGN properties they are found at the top end of the mass distribution of $z \simeq 6.2$ sources compiled in T11, but at the low end in terms of $L/L_{\rm Edd}$. Their SFRs are somewhat in between our FIR-bright and FIR-faint objects. We include these 3 sources in our Figure 5.1. It is somewhat unexpected that this $z \sim 6.6$ sample fits so well within our own, however a much larger and uniform sample from $z > 6.6$ is required to draw conclusions.

Assuming that the stellar mass of the quasar host galaxies grows only due to the formation of new stars (i.e., neglecting possible mergers), we can use our SFR estimates from Section 3.3 to calculate the growth rate of $M_\star$, i.e., $\dot{M}_\star$. The instantaneous growth rate of the black holes can be computed as the mass accreted onto the black hole which does not convert into energy: $\dot{M}_{BH} = \frac{1-\eta}{\eta}\frac{L_{bol}}{c^2}$, where L_{bol} is the bolometric luminosity from T11 using the rest-frame UV continuum emission. We assume the radiative efficiency to be $\eta = 0.1$.

We find that all systems have $\dot{M}_{BH}/\dot{M}_\star > 1/200$ and typical values are found to be $\sim 1/54$ (see Table 4.1 Galaxy Properties II), with the FIR-bright and FIR-faint systems having medians of $\dot{M}_{BH}/\dot{M}_\star \simeq 1/71$ and $1/27$ respectively.

Assuming that the calculated instantaneous growth rates continue for a period of time, we can determine the migration that our sources would undergo on the M_{BH} vs $M_\star$ plot. The time span needs to be determined under reasonable assumptions. Typical starformation time scales derived at lower redshifts might not be applicable to our sample. Using the determined M_g and SFRs we can find the depletion time for the observed reservoir of gas. This is found to be between 20 to 100 Myr. Hence, we will adopt a general time span of 50 Myr.

As already discussed, because of the stochastic nature of AGN activity, with duty cycles shorter than those of star-formation by one or perhaps up to two orders of magnitude (e.g., Hickox et al., 2014; Volonteri et al., 2015; Stanley et al., 2015), the instantaneous $\dot{M}_{BH}$ values measured for single objects might not be the best proxy to characterize black hole growth over the time required for the build up a sizable stellar mass due to star formation. Instead, the value averaged over our entire sample will result in better determination of the 'typical' $\dot{M}_{BH}$. The resulting 'growth tracks' are shown in Figure 5.1. We also obtained the means of $\dot{M}_{BH}$ and $\dot{M}_\star$ separately for the FIR-bright and FIR-faint subsamples and have plotted them in Figure 5.1. For roughly half of our objects these tracks suggest a larger future growth of stellar mass over BH mass, which is necessary to bring them closer to the local population of elliptical galaxies.

5.2 Major mergers among hosts

Different lines of evidence suggest that mergers among gas-rich galaxies should drive the most luminous AGN and the most powerful starformation of their hosts. This is proposed by numerical simulations (Hopkins et al., 2005, 2008) and also backed by observations at low and high-z (Treister et al., 2012; Glikman et al., 2015; Koss et al., 2018). Thus our initial expectations were to find that our ALMA observations would show that the FIR-bright sources are powered by major mergers of gas-rich galaxies, and that the FIR-faint sources, found closer to the main sequence of galaxies, could be evolving through a secular process or also involved in mergers. The evidence would emerge from the presence of close companions to our quasars.

We find that of the $\sim$ 28 % host galaxies with companions the majority are FIR-faint sources (1 FIR-bright and 4 FIR-faint). One FIR-bright source, J1404, presents an unusual [C II] double peak that could signal a late stage merger. Bischetti et al. (2018) found three companions around their targeted $z = 4.4$ quasar, two of which have double-peaked line emission, while in Willott et al. (2017), the high spectral and spatial resolution allows them to attribute different peaks in the [C II] line to the quasar source, a 5 kpc separated companion, and a "central excess" component between the two.

The lack of companions to FIR-bright quasars is in fact problematic, as it is usually assumed major mergers between gas-rich galaxies to be the triggering mechanism for star-bursting galaxies. Note, however, that recent ALMA observations at $z \sim 4.5$, suggest that minor-mergers might also locate systems above the main sequence (Gómez-Guijarro et al., 2018).

The preference for companions in FIR-faint sources could then be explained if these correspond to very early stages in the merger process, while the FIR-bright systems correspond to much later stages, when the progenitor galaxies are no longer resolved by our ALMA observations. The lack of disturbances in the velocity fields of our systems does not oppose this argument, as observations of the ISM in low-z mergers demonstrate that the central core of mergers rapidly settles into a rotating-dominated system (Ueda et al., 2014). Of note is that the closest companion SMG in our sample is for the FIR-bright object J1511, separated from the QSO by 14 kpc. This further feeds into the theory that the FIR-bright objects are in later stage mergers, with on disk or nearby SMGs (J1511), while the FIR-faint sources are still in the early stages with companion SMGs much more separated and detectable.

The lack of clear, 'on-going' mergers among our systems could be explained as a sample bias since our quasars were optically selected. Glikman et al. (2015) has shown that for a sample of 2MASS selected dust-reddened quasars at $z \sim 2$, 8/10 hosts show clear evidence for very close, interacting companions. Similar results were found by Urrutia et al. (2008) for dust-reddened quasars at $z \sim 0.4 - 1.0$. The nuclei are so heavily dust-enshrouded that HST follow up clearly revealed the perturbed hosts. As argued in Díaz-Santos et al. (2018), where they consider a hot dust obscured galaxy with three accreting companions, the merger-driven accretion of neighbor galaxies can obscure the SMBH while at the same time providing the influx of material necessary to facilitate SF. These types of quasars would not be found in our parent sample. It is then possible that the distinct populations observed in the $L_{\rm AGN}$-$L_{\rm SF}$ plane (Figure 3.6) reflect the properties of the very early and very late mergers just mentioned.

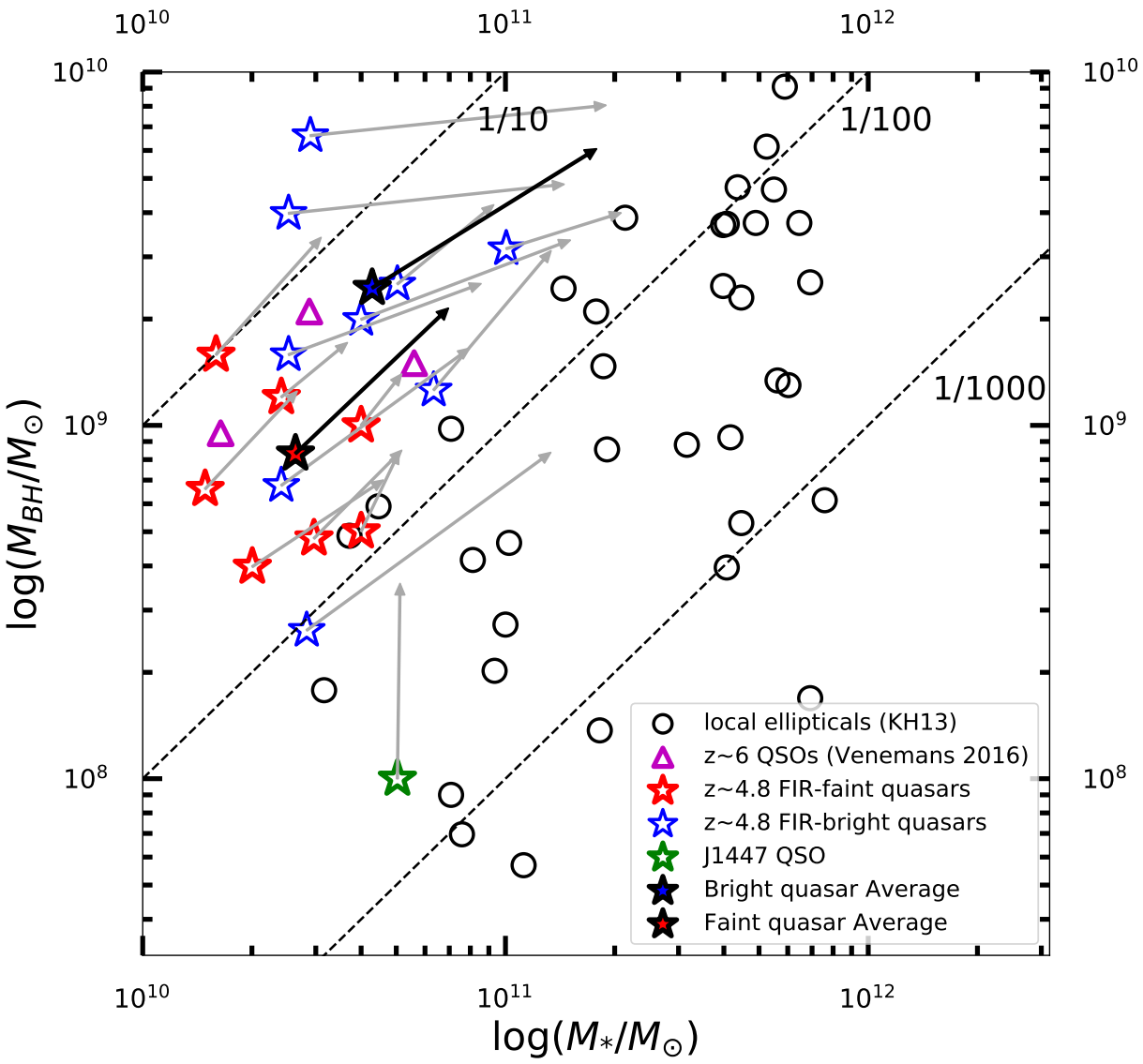

Figure 5.1: Black hole masses, $M_{\rm BH}$, vs. host galaxy stellar masses, $M_\star$, for our sample of $z \sim 4.8$ quasars. FIR-bright objects are marked with blue stars, FIR-faint objects are marked with red. For comparison we also plot a sample of $z \simeq 0$ elliptical galaxies taken from Kormendy & Ho (2013) shown as black circles, as well as the three sources from Venemans et al. (2016) as purple triangles. The dotted diagonal lines trace different constant BH-to-host mass ratios. Grey arrows indicate the possible evolution in both the BH and stellar components, assuming constant mass growth rates over a period of 50 Myr. Filled stars with black arrows indicate average values and growth for both FIR-faint and bright objects. Our plotted sources have a typical error of 0.44 dex for $M_\star$ (from our own estimates) and 0.4 dex for $M_{\rm BH}$ (derived in T11).

Chapter 6

Conclusion

We have presented band-7 ALMA observations for 18 luminous, unobscured quasars at $z \simeq 4.8$, which are divided into *Herschel*/SPIRE detected (FIR-bright) and *Herschel*/SPIRE undetected (FIR-faint) systems. The data probes the rest-frame far-IR continuum emission that arises from dust heated by SF in the host galaxies of the quasars, and the [C II] $\lambda 157.74\,\mu$m emission line from the host ISM. The ALMA observations resolve the continuum- and line-emitting regions on scales of ~ 2 kpc which allows us to study the host morphology and kinematics as well as detect nearby companion sources. We have observed 18/38 of our original sample with ALMA.

In Chapter 2 we found that 5/18 of our quasars have companions, four of the quasars are FIR-faint and one is FIR-bright. The companions are separated by 14 - 60 kpc from their host QSO. The lack of companions for the remainder of our quasar hosts may suggest that processes other or besides major mergers are driving the significant SF activity and fast SMBH growth in these systems. However, it is important to note that the percentage of our objects with companions, $28^{+.14}_{-.11}\%$, is slightly higher than other high-redshift studies ($16^{+.11}_{-0.8}\%$ in Decarli et al. 2018). This relatively low percentage of companions does not support the theory that all highly-luminous quasars and SF-host galaxies are being fueled by the merger driven scenario we discussed in Chapter 1. Alternatively, the systems could be observed at very different stages of the merger process, with most FIR-faint sources found at the early stages, while FIR-bright are found at very late phases.

In Chapter 3 we analyzed in detail the emission of our sources, using the LOSVD of the [C II] line to create velocity maps. We found that all but one of our velocity maps show no indication of major merger activity in our QSOs, the exception being J2057 with a perturbed companion and possible tidal tail. However other radio studies (Ueda et al., 2014) also fail to clearly discern merger activity from CO maps in known merger remnants showing that intensity and velocity maps can hide perturbed conditions, expect in the most extreme cases. Therefore, we are not able to detect possible late or on disk mergers. Additionally in Chapter 3 we used the underlying continuum emission to construct SEDs of our objects from which we calculate SFRs assuming the Chabrier (2003) IMF. The quasar hosts have a SFR rate of $\sim 90 - 3200 M_\odot\,\mathrm{yr}^{-1}$, while the companions are forming stars at rates of $69 - 542\,M_\odot\,\mathrm{yr}^{-1}$ which is comparable to, or in specific cases greater, than their quasar host SFRs.

By using the previously mentioned emission properties of our host galaxies, in Chapter 4 we found the dynamical, dust, and gas masses. The dynamical masses of the quasar hosts with nearby companions, estimated from the [C II] lines, are within a factor of ~ 3 of the masses of the interacting companions, supporting an interpretation of these interactions as major mergers. We also find that the gas mass is comparable to the dynamical mass, suggesting that some of them could be kinematically dominated by the ISM component. Assuming $f_{gas} = M_{gas}/M_{\rm dyn} = 0.6$ we derive M_* for the hosts. By comparing the derived stellar mass to the SFRs of Chapter 3, we show that both the FIR-bright and FIR-faint objects lie above the MS. When comparing $L_{\rm AGN}$ vs $L_{\rm SF}$ we see that the two subsamples are clearly separated, while the SFRs themselves are a continuous distribution. In the merger driven scenario we can interpret the separation of the two subsamples as different stages of mergers, with the FIR-bright objects in later stage or on-disk mergers, previously mentioned, or nearby SMGs such as J1511. These late stage mergers would fuel the higher accretion and star formation rates that place the FIR-bright subsample above the FIR-faint objects. At the same time the FIR-faint sources are in early stages of mergers with companion SMGs more separated and detectable, thus still to evolve into the full merger regime in terms of accretion and SFRs.

Finally, in Chapter 5 we compared the accretion rate of the SMBHs to the SFRs of our hosts and see that within a short duty cycle our SMBHs will be generally consistent with the local range of $M_{\rm BH}$, while the [C II]-based dynamical host masses are generally lower than what is expected from the locally observed $M_{\rm BH}/M_*$ mass ratio.

Acknowledgments
This work makes use of the following ALMA data: ADS/JAO.ALMA#2013.1.01153.S., ADS/JAO.ALMA#2016.1.01515.S. ALMA is a partnership of ESO (representing its member states), NSF (USA) and NINS (Japan), together with NRC (Canada) and NSC and ASIAA (Taiwan) and KASI (Republic of Korea), in cooperation with the Republic of Chile. The Joint ALMA Observatory is operated by ESO, AUI/NRAO and NAOJ.

Bibliography

Adelman-McCarthy, J. K., Agüeros, M. A., Allam, S. S., et al. 2008, The Astrophysical Journal Supplement Series, 175, 297

Aird, J., Nandra, K., Laird, E. S., et al. 2010, MNRAS, 401, 2531

Allen, S. W., Dunn, R. J. H., Fabian, A. C., Taylor, G. B., & Reynolds, C. S. 2006, MNRAS, 372, 21

Aravena, M., Decarli, R., Walter, F., et al. 2016a, ApJ, 833, 68

—. 2016b, ApJ, 833, 71

Aravena, M., Spilker, J. S., Bethermin, M., et al. 2016c, MNRAS, 457, 4406

Banados, E., Decarli, R., Walter, F., et al. 2015, ApJ, 805, L8

Banados, E., Venemans, B. P., Mazzucchelli, C., et al. 2018, Nature, 553, 473

Banerji, M., Carilli, C. L., Jones, G., et al. 2017, MNRAS, 465, 4390

Beelen, A., Cox, P., Benford, D. J., et al. 2006, ApJ, 642, 694

Bischetti, M., Piconcelli, E., Feruglio, C., et al. 2018, ArXiv e-prints, arXiv:1804.06399

Bouwens, R. J., Illingworth, G. D., Oesch, P. A., et al. 2015, ApJ, 803, 34

Bussmann, R. S., Riechers, D., Fialkov, A., et al. 2015, ApJ, 812, 43

Carniani, S., Maiolino, R., De Zotti, G., et al. 2015, A&A, 584, A78

Chabrier, G. 2003, Publications of the Astronomical Society of the Pacific, 115, 763

Chary, R., & Elbaz, D. 2001, ApJ, 556, 562

Coatman, L., Hewett, P. C., Banerji, M., & Richards, G. T. 2016, MNRAS, 461, 647

Costa, T., Sijacki, D., Trenti, M., & Haehnelt, M. G. 2014, MNRAS, 439, 2146

Darvish, B., Scoville, N. Z., Martin, C., et al. 2018, ApJ, 860, 111

De Rosa, G., Decarli, R., Walter, F., et al. 2011, ApJ, 739, 56

De Rosa, G., Venemans, B. P., Decarli, R., et al. 2014, ApJ, 790, 145

De Vis, P., Jones, A., Viaene, S., et al. 2019, A&A, 623, A5

Decarli, R., Walter, F., Venemans, B. P., et al. 2017, Nature, 545, 457

—. 2018, ApJ, 854, 97

Delvecchio, I., Gruppioni, C., Pozzi, F., et al. 2014, MNRAS, 439, 2736

Dessauges-Zavadsky, M., Zamojski, M., Rujopakarn, W., et al. 2017, A&A, 605, A81

Di Matteo, T., Springel, V., & Hernquist, L. 2005, Nature, 433, 604

Díaz-Santos, T., Assef, R. J., Blain, A. W., et al. 2016, ApJL, 816, L6

—. 2018, Science, 362, 1034

Draine, B. T., Dale, D. A., Bendo, G., et al. 2007, ApJ, 663, 866

Dunne, L., Eales, S., Edmunds, M., et al. 2000, MNRAS, 315, 115

Duras, F., Bongiorno, A., Piconcelli, E., et al. 2017, A&A, 604, A67

Ferrarese, L., & Merritt, D. 2000, ApJL, 539, L9

Flewelling, H. A., Magnier, E. A., Chambers, K. C., et al. 2016, arXiv e-prints, arXiv:1612.05243

Fujimoto, S., Ouchi, M., Ono, Y., et al. 2016, The Astrophysical Journal Supplement Series, 222, 1

Gaia Collaboration, Brown, A. G. A., Vallenari, A., et al. 2018, A&A, 616, A1

Ge, X., Zhao, B.-X., Bian, W.-H., & Frederick, G. R. 2019, AJ, 157, 148

Glikman, E., Simmons, B., Mailly, M., et al. 2015, ApJ, 806, 218

Gnerucci, A., Marconi, A., Cresci, G., et al. 2011, A&A, 528, A88

Goicoechea, J. R., Chavarría, L., Cernicharo, J., et al. 2015, ApJ, 799, 102

Gómez-Guijarro, C., Toft, S., Karim, A., et al. 2018, ApJ, 856, 121

Gowardhan, A., Riechers, D., Pavesi, R., et al. 2019, ApJ, 875, 6

Gültekin, K., Richstone, D. O., Gebhardt, K., et al. 2009, The Astrophysical Journal, 698, 198–221. http://dx.doi.org/10.1088/0004-637X/698/1/198

Hatziminaoglou, E., Farrah, D., Humphreys, E., et al. 2018, MNRAS, 480, 4974

Hayward, C. C., Chapman, S. C., Steidel, C. C., et al. 2018, MNRAS, 476, 2278

Hewett, P. C., & Wild, V. 2010, MNRAS, 405, 2302

Hickox, R. C., Mullaney, J. R., Alexander, D. M., et al. 2014, ApJ, 782, 9

Hodge, J. A., Karim, A., Smail, I., et al. 2013, ApJ, 768, 91

Hopkins, P. F., Hernquist, L., Cox, T. J., & Kereš, D. 2008, ApJS, 175, 356

Hopkins, P. F., Hernquist, L., Martini, P., et al. 2005, ApJL, 625, L71

Hopkins, P. F., Richards, G. T., & Hernquist, L. 2007, ApJ, 654, 731

Hopkins, P. F., Somerville, R. S., Hernquist, L., et al. 2006, ApJ, 652, 864

Ivison, R. J., Swinbank, A. M., Swinyard, B., et al. 2010, A&A, 518, L35

Kennicutt, Robert C., J. 1989, ApJ, 344, 685

Kormendy, J., & Ho, L. C. 2013, Annual Review of Astronomy and Astrophysics, 51, 511

Koss, M. J., Blecha, L., Bernhard, P., et al. 2018, Nature, 563, 214

Kurk, J. D., Walter, F., Fan, X., et al. 2007, ApJ, 669, 32

Lani, C., Netzer, H., & Lutz, D. 2017, MNRAS, 471, 59

Leipski, C., Meisenheimer, K., Walter, F., et al. 2014, ApJ, 785, 154

Lian, J., Thomas, D., & Maraston, C. 2018, MNRAS, 481, 4000

Lutz, D. 2014, ARA&A, 52, 373

Lutz, D., Mainieri, V., Rafferty, D., et al. 2010, ApJ, 712, 1287

Lutz, D., Berta, S., Contursi, A., et al. 2016, A&A, 591, A136

Madau, P., & Dickinson, M. 2014, ARA&A, 52, 415

Magnelli, B., Saintonge, A., Lutz, D., et al. 2012, A&A, 548, A22

Makarov, V. V., Frouard, J., Berghea, C. T., et al. 2017, ApJL, 835, L30

Mason, M., Brotherton, M. S., & Myers, A. 2017, MNRAS, 469, 4675

Mazzucchelli, C., Ba∼nados, E., Venemans, B. P., et al. 2017, ApJ, 849, 91

McMullin, J. P., Waters, B., Schiebel, D., Young, W., & Golap, K. 2007, in Astronomical

Society of the Pacific Conference Series, Vol. 376, Astronomical Data Analysis Software and Systems XVI, ed. R. A. Shaw, F. Hill, & D. J. Bell, 127

Mejía-Restrepo, J. E., Trakhtenbrot, B., Lira, P., Netzer, H., & Capellupo, D. M. 2016, MNRAS, 460, 187

Miettinen, O., Delvecchio, I., Smolčić, V., et al. 2017, A&A, 606, A17

Mor, R., & Netzer, H. 2012, MNRAS, 420, 526

Mor, R., Netzer, H., Trakhtenbrot, B., Shemmer, O., & Lira, P. 2012, ApJ, 749, L25

Nesvadba, N. P. H., Lehnert, M. D., De Breuck, C., Gilbert, A. M., & van Breugel, W. 2008, A&A, 491, 407

Netzer, H. 2009, MNRAS, 399, 1907

Netzer, H., Lani, C., Nordon, R., et al. 2016, ApJ, 819, 123

Netzer, H., Mor, R., Trakhtenbrot, B., Shemmer, O., & Lira, P. 2014, ApJ, 791, 34

Netzer, H., Lutz, D., Schweitzer, M., et al. 2007, ApJ, 666, 806

Nguyen, N. H., Lira, P., Trakhtenbrot, B., et al. 2020, arXiv:2003.00525

Orosz, G., & Frey, S. 2013, A&A, 553, A13

Pentericci, L., Carniani, S., Castellano, M., et al. 2016, ApJL, 829, L11

Planck Collaboration, Adam, R., Aghanim, N., et al. 2016, A&A, 596, A108

Pognan, Q., Trakhtenbrot, B., Sbarrato, T., Schawinski, K., & Bertemes, C. 2020, MNRAS, 79

Rémy-Ruyer, A., Madden, S. C., Galliano, F., et al. 2014, A&A, 563, A31

Richards, G. T., Vanden Berk, D. E., Reichard, T. A., et al. 2002, AJ, 124, 1

Rosario, D. J., Santini, P., Lutz, D., et al. 2012, A&A, 545, A45

Salpeter, E. E. 1964, ApJ, 140, 796

Schinnerer, E., Groves, B., Sargent, M. T., et al. 2016, ApJ, 833, 112

Schneider, R., Bianchi, S., Valiante, R., Risaliti, G., & Salvadori, S. 2015, A&A, 579, A60

Schreiber, C., Pannella, M., Elbaz, D., et al. 2015, A&A, 575, A74

Schweitzer, M., Lutz, D., Sturm, E., et al. 2006, ApJ, 649, 79

Scoville, N., Sheth, K., Aussel, H., et al. 2016, ApJ, 820, 83

Scudder, J. M., Oliver, S., Hurley, P. D., et al. 2016, MNRAS, 460, 1119

Shankar, F., Weinberg, D. H., & Miralda-Escudé, J. 2009, ApJ, 690, 20

Shao, L., Lutz, D., Nordon, R., et al. 2010, A&A, 518, L26

Shen, Y., Brandt, W. N., Richards, G. T., et al. 2016, ApJ, 831, 7

Siebenmorgen, R., Heymann, F., & Efstathiou, A. 2015, A&A, 583, A120

Silk, J., & Rees, M. J. 1998, A&A, 331, L1

Somerville, R. S., Hopkins, P. F., Cox, T. J., Robertson, B. E., & Hernquist, L. 2008, MNRAS, 391, 481

Stanley, F., Harrison, C. M., Alexander, D. M., et al. 2015, MNRAS, 453, 591

Stark, D. P., Ellis, R. S., Bunker, A., et al. 2009, ApJ, 697, 1493

Sulentic, J. W., del Olmo, A., Marziani, P., et al. 2017, A&A, 608, A122

Sun, M., Xue, Y., Richards, G. T., et al. 2018, ApJ, 854, 128

Targett, T. A., Dunlop, J. S., & McLure, R. J. 2012, MNRAS, 420, 3621

Tomczak, A. R., Quadri, R. F., Tran, K.-V. H., et al. 2016, ApJ, 817, 118

Trakhtenbrot, B., Lira, P., Netzer, H., et al. 2017, ApJ, 836, 8

Trakhtenbrot, B., & Netzer, H. 2012, MNRAS, 427, 3081

Trakhtenbrot, B., Netzer, H., Lira, P., & Shemmer, O. 2011, ApJ, 730, 7

Treister, E., Schawinski, K., Urry, C. M., & Simmons, B. D. 2012, ApJ, 758, L39

Ueda, J., Iono, D., Yun, M. S., et al. 2014, ApJS, 214, 1

Urrutia, T., Lacy, M., & Becker, R. H. 2008, ApJ, 674, 80

Venemans, B. P., Walter, F., Zschaechner, L., et al. 2016, ApJ, 816, 37

Venemans, B. P., McMahon, R. G., Walter, F., et al. 2012, ApJ, 751, L25

Venemans, B. P., Ba∼nados, E., Decarli, R., et al. 2015, ApJ, 801, L11

Venemans, B. P., Walter, F., Decarli, R., et al. 2017, ApJ, 851, L8

Vietri, G., Piconcelli, E., Bischetti, M., et al. 2018, A&A, 617, A81

Volonteri, M., Capelo, P. R., Netzer, H., et al. 2015, MNRAS, 449, 1470

Wang, R., Wagg, J., Carilli, C. L., et al. 2013, ApJ, 773, 44

Wang, R., Wu, X.-B., Neri, R., et al. 2016, ApJ, 830, 53

Wilkinson, A., Almaini, O., Chen, C.-C., et al. 2017, MNRAS, 464, 1380

Williams, R. J., Maiolino, R., Santini, P., et al. 2014, MNRAS, 443, 3780

Willott, C. J., Bergeron, J., & Omont, A. 2015, ApJ, 801, 123

—. 2017, ApJ, 850, 108

Willott, C. J., Omont, A., & Bergeron, J. 2013, ApJ, 770, 13

Willott, C. J., Albert, L., Arzoumanian, D., et al. 2010, AJ, 140, 546

Wu, X.-B., Wang, F., Fan, X., et al. 2015, Nature, 518, 512

Wyithe, J. S. B., & Loeb, A. 2012, MNRAS, 425, 2892

York, D. G., Adelman, J., Anderson, Jr., J. E., et al. 2000, AJ, 120, 1579